# Single-nucleus transcriptomic analyses reveal microglial activation underlying cerebellar degeneration in Ataxia Telangiectasia

**Authors:**
Jenny Lai[1,2,3,4], Junho Kim[1,2,3], Ailsa M. Jeffries[5], Allie Tolles[5], Thomas W. Chittenden[1,6], Patrick G. Buckley[7], Timothy W. Yu[1,2,3,4], Michael A. Lodato[5], Eunjung Alice Lee[1,2,3,4]

**Affiliations:**

1. Division of Genetics and Genomics, Department of Pediatrics, Boston Children's Hospital, Boston, MA, 02215, USA
2. The Manton Center for Orphan Disease Research, Boston Children's Hospital, Boston, MA, 02215, USA
3. Broad Institute of MIT and Harvard, Cambridge, MA, 02142, USA
4. Program in Neuroscience, Harvard University, Boston, MA, 02115, USA
5. Department of Molecular, Cell, and Cancer Biology, University of Massachusetts Medical School, Worcester, MA, 01605, USA
6. Computational Statistics and Bioinformatics Group, Genuity AI Research Institute, Genuity Science, Boston, MA 02114, USA
7. Genuity Genomics Centre, Genuity Science, Dublin, D18 K7W4, Ireland

*To whom correspondence should be addressed. E-mail:
EAlice.Lee@childrens.harvard.edu and Michael.Lodato@umassmed.edu

## Abstract

While *ATM* loss-of-function has long been identified as the genetic cause of Ataxia Telangiectasia (AT), how this genetic mutation leads to selective and progressive cerebellar degeneration of Purkinje and granule cells remains unknown. We performed single-nucleus RNA-sequencing of the human cerebellum and prefrontal cortex from individuals with AT and matched unaffected controls to identify AT-associated transcriptomic changes in a cell-type- and brain-region-specific manner. We provide the largest single-nucleus transcriptomic atlas of the adult human cerebellum to-date (126,356 nuclei), identify upregulation of apoptotic and ER stress pathways in Purkinje and granule neurons, and uncover strong downregulation of calcium ion homeostasis genes in Purkinje neurons. Our analysis reveals prominent inflammation of microglia in AT cerebellum with transcriptional signatures similar to aging and neurodegenerative microglia, and suggests that microglia activation precedes Purkinje and granule neuron death in disease progression. Our data implicates a novel role of microglial activation underlying cerebellar degeneration in AT.

## Introduction

Selective degeneration of the cerebellum occurs in genetic ataxias such as Ataxia Telangiectasia (AT). However, the mechanisms underlying cerebellar degeneration remain poorly understood. AT is an autosomal recessive multi-system disorder caused by mutations in the gene *ATM*, a multifunctional kinase known for its role in DNA damage response to double strand breaks (DSB)[1,2]. DNA damage leads to ATM activation, which phosphorylates downstream regulators of cell cycle arrest, DNA repair, and apoptosis[3]. Recently, metabolic roles of *ATM* have also emerged. ATM can form a dimer that mediates mitochondrial redox sensing and regulates antioxidant capacity[4]. Moreover, *ATM* deficiency leads to upregulation of autophagy and perinuclear accumulation of lysosomes, implicating *ATM* in lysosomal trafficking[5].

While *ATM* has roles in diverse cellular functions, it remains unclear how *ATM* loss-of-function leads to selective and progressive degeneration of Purkinje and granule neurons in the cerebellum. Animal models of AT unfortunately fail to recapitulate the cerebellar degeneration found in humans[6], but bulk transcriptomic analyses of human brain tissue and neuronal models have begun to offer some insights into dysregulated pathways in AT. Expression of *ITPR1,* a calcium channel that is highly expressed in Purkinje cells and is associated with spinocerebellar ataxias, is significantly altered in AT cerebellum[7]. Transcriptome analyses of induced pluripotent stem cell-derived cerebellar-like neurons from individuals with AT and controls have also revealed alterations in pathways related to synaptic vesicle cycling, oxidative stress, and insulin secretion[8]. However, it remains unresolved whether bulk transcriptomic changes reflect loss of certain cell types in AT, or perturbation of cellular functions in specific cell types, as hinted by recent studies beginning to interrogate the effects of *ATM* deficiency on glia[9,10]. Thus, there is a need for greater understanding of the regional and cell-type-specific effects of *ATM* deficiency that may provide insight on mechanisms that cause cerebellar degeneration.

Single-cell technology has provided insight on the cell-type-specific effects of neurological diseases including Alzheimer's disease (AD), Huntington's disease, Multiple Sclerosis, Autism, and Major Depressive Disorder[11–15]. However, data from human adult cerebellum in health and degeneration has not yet been explored. Here, we present the largest single-nucleus transcriptomic atlas of adult human cerebellum and the first atlas of cerebellar degeneration to-date. We profiled 126,356 nuclei from the postmortem human cerebellar vermis of six AT and seven matched control individuals. In addition, we profiled 86,354 nuclei from postmortem human prefrontal cortex (PFC) from two AT and two matched control individuals. We annotated major cell types in the human cerebellum and PFC, and identified cell type proportion changes between AT and controls. We also demonstrated cell-type-specific expression of cerebellar ataxia-associated disease genes, some of which were significantly dysregulated in AT Purkinje neurons, supporting a convergence in disease

pathophysiology underlying several hereditary ataxias. We analyzed the cell-type-specific molecular pathways perturbed in AT across these brain regions, revealing prominent and widespread activation of inflammatory pathways in cerebellar microglia. Moreover, our analyses implicate this microglial activation in Purkinje and granule cell degeneration. Taken together, our data suggests that activated microglia are central to AT pathophysiology and cerebellar degeneration.

## Results

### Single-nucleus RNA-seq profiling of AT human cerebellum and prefrontal cortex

AT presents with prominent loss of motor coordination associated with early selective atrophy of the cerebellum. To investigate cell type and region-specific perturbations in AT, we performed single-nucleus RNA-sequencing (snRNA-seq) of human postmortem tissues from the cerebellar vermis (the region with the most prominent atrophy in AT[16]) and prefrontal cortex (PFC) (Figure 1A). We profiled six cerebella from neuropathologically confirmed AT cases (Table S3) and seven control cerebella, as well as matched AT and control PFC from two cases each. The ages of the AT cases ranged from 19 to 50 years old (mean age 28 years). All cases were balanced for age, sex, RNA integrity number, and postmortem interval (Tables S1-S2). In total, we sequenced 233,756 nuclei (97,612 AT; 136,144 control) from human cerebellum and 111,773 nuclei (31,470 AT; 80,303 control) from human PFC. After quality control and doublet filtering, we used 126,356 cerebellar nuclei (51,297 AT; 75,059 control) and 86,354 PFC nuclei (16,979 AT; 69,375 control) for downstream analysis[17–19] (Figures S1A-D). On average, we were able to resolve 869 expressed genes and 1,378 unique transcripts per cerebellar nucleus, and 1,352 genes and 2,253 transcripts per PFC nucleus, in line with yields from previous human postmortem snRNA-seq brain studies[11–15].

To genetically confirm the diagnoses of AT, we performed variant calling on whole genome sequencing (WGS) data and snRNA-seq data from the AT cases. For all six cases, variants in *ATM* with evidence of pathogenicity in ClinVar were identified (Table S4, Figure S2). All cases showed evidence of compound heterozygosity except one case (4663) that was homozygous for a pathogenic splice variant. Thus, all AT cases were putatively fully genetically confirmed.

To distinguish cerebellar cell types, we used Seurat[17] to perform graph-based clustering with the Leiden algorithm and annotated clusters based on the expression of canonical marker genes. 10 major cell types were identified, including the cerebellum specific granule cells (*RIMS1, GRM4)*, Purkinje cells (*ITPR1, CALB1)*, and Bergmann-glia (*TUBB2B, AQP4)*, as well as interneurons (*GAD1, PVALB)*, astrocytes (*TTN, AQP1)*, oligodendrocytes (*PLP1, MBP)*, oligodendrocyte precursor cells (OPC)

(*PDGFRA, OLIG1)*, microglia (*CD74, CSF1R)*, endothelial cells (*CLDN5, VWF)*, and fibroblasts (*DCN, APOD)* (Figures 1B-C).

**Single-nucleus RNA-seq recapitulates neuropathological hallmarks and reveals increased glial populations in AT cerebellum**

Next, to understand the patterns of cerebellar cell loss in AT, we examined the cell type proportions in AT compared to controls. Due to the negative covariance structure of compositional data—as one feature increases, the other features must decrease—we implemented Dirichlet multinomial modeling using Hamiltonian Monte Carlo (DMM-HMC) to estimate the cell type proportions in AT and control[20]. We generated multinomial distributions of cell type proportions for each sample based on the nuclei counts, and used these to construct a Dirichlet distribution of cell type proportions in AT and controls. To determine the relative shift in abundance of each cell type in AT versus control, we subtracted the control posterior probability distribution of proportions from the AT distribution (Figure 1D). Granule cells were significantly decreased in AT (Figure 1E, 89% credibility interval). Purkinje cells were reduced in abundance, although not significantly, possibly due to individual sample variability and decreased power for detecting changes in rare cell types. In addition, astrocytes, Bergmann-glia, microglia, and oligodendrocytes showed significant increases in AT compared to control (Figure 1E, 89% credibility interval). In contrast, permutation testing of disease labels (AT versus control) showed no significant differences for any cell type, as expected (permutation n=500, Figure S1E).

These results are consistent with human AT neuropathology autopsy reports, which describe granule and Purkinje cell atrophy and gliosis in the cerebellum (Table S3), and reveal significant increases in astrocytes, Bergmann-glia, oligodendrocytes, and microglia contributing to gliosis in AT.

**Monogenic cerebellar disease genes are expressed in specific cell types**

Next, we characterized the expression of *ATM* across cell types in the cerebellum and PFC to gain insight on disease mechanisms. Remarkably, *ATM* had the highest expression in microglia in adult human cerebellum and PFC (Figure 2A). To investigate human developmental expression patterns, we profiled the expression of *ATM* in a snRNA-seq dataset of human fetal cerebellum[21], which also revealed the highest expression of *ATM* in microglia (Figure 2A). Taken together, these data suggest a particularly important role of *ATM* in microglia throughout cerebellar development.

Given that *ATM* is enriched in microglia, we wanted to see whether additional hereditary ataxia genes are enriched in specific cerebellar cell types. We curated a list of genes implicated in human hereditary ataxias using the Online Mendelian Inheritance in Man (OMIM) database (Table S5) and profiled their expression in specific cell types.

We found that like *ATM*, most hereditary ataxia disease genes demonstrate cell-type-specific patterns of expression (Figure 2B; Bonferroni adjusted p-value < 0.05, t-test). Cerebellar disease gene expression was most commonly enriched in Purkinje cells, including the potassium and calcium ion related genes *KCND3, PRKCG, CACNA1G, ITPR1, TRPC3,* and *KCNC3*. Microglia also showed enriched expression of several ataxia disease genes (*ATM, TPP1, SETX,* and *VPS13D*) (Figure 2B).

Mouse models of AT do not develop cerebellar atrophy as found in humans. To examine whether species differences in cell-type-specific expression of disease genes may underlie phenotypic differences, we profiled cerebellar disease gene expression across cell types using single-cell RNA-seq data from adult mouse cerebellum[22]. Disease gene expression enrichment in human Purkinje neurons was largely conserved in mice (Figure 2B). We used the cosine similarity metric to assess the correlation of cell type expression profiles for cerebellar disease genes between humans and mice. Granule cells, oligodendrocytes, astrocytes, and Purkinje neurons were the most correlated between humans and mice, while microglia were the least correlated (Figure 2C). Moreover, the human microglia enriched genes *Atm, Setx,* and *Vps13d* had relatively depleted expression in murine microglia compared to other cell types (Figure 2B). Notably, *Atm, Setx,* and *Vps13d* mouse models do not develop cerebellar atrophy[6,23,24], suggesting that these expression differences may contribute to human-specific disease manifestation.

**Transcriptional dysregulation across cerebellar cell types in AT**

To investigate the cell types and molecular pathways that are most perturbed in AT, we performed differential gene expression analysis between AT and control for each cell type. Genes with a |log2 fold-change| > 0.50 and a false discovery rate (FDR) < 0.05 were considered as significantly differentially expressed genes (DEGs) (Table S6). Astrocytes, microglia, and oligodendrocytes had remarkably high numbers of DEGs (1,631, 1,577, 1,563 respectively) while granule cells had the least (265) (Figure 3A). These data suggest that while granule cells degenerate in AT, their gene expression program is less dysregulated than other cerebellar cell types such as glia.

To estimate the information gain from single-nucleus analysis compared to bulk RNA-seq, we performed differential gene expression analysis on ‘pseudobulk’ data generated by summing read counts across all cells for each sample. In total, pseudobulk analysis identified 250 upregulated and 111 downregulated DEGs (FDR < 0.05, |log2 fold-change| > 0.50), representing a recovery of <25% of the DEGs identified by snRNA-seq analysis (Figure 3B). Rare cell types such as microglia had the least recovery of DEGs by bulk analysis (<13%), while granule cells, the most abundant cell type in the cerebellum, had the highest recovery (21.7%). Overall, nearly 50% of the single-nucleus DEGs were cell-type-specific (Figure 3C). At increasing log2 fold-change thresholds, the proportion of DEGs that were cell-type specific increased, suggesting

that the strongest transcriptional alterations in AT are cell-type-specific (Figure 3D). Microglia and Purkinje cells had the most cell-type-specific DEGs, suggesting unique roles in AT pathogenesis (Figure 3E).

Next, we performed Gene Ontology (GO) analysis on the DEGs found in each cell type to gain insight into the biological processes dysregulated in AT. Consistent with the loss of Purkinje and granule cells in AT, both cell types had significant upregulation of apoptotic signaling pathways (Figures 4A-B, Figure S3A, Table S7). Purkinje cells upregulated genes involved in responding to extrinsic apoptotic signals. In contrast, granule neurons upregulated genes involved in intrinsic apoptotic signaling and DNA damage response. AT Purkinje and granule cells also upregulated genes involved in ribosome assembly and biogenesis, which has been observed in several studies of aging brains[25,26]. Loss of *ATM* in microglia led to upregulation of microglial cell activation, phagocytosis, and defense response to virus genes (Figure 4C). Additionally, AT microglia demonstrated strong and specific enrichment of both innate and adaptive immune related processes among its upregulated genes, including cytokine production, leukocyte mediated cytotoxicity, and T cell mediated cytotoxicity. The cytokine-mediated signaling pathway was significantly upregulated in both Purkinje and granule neurons in AT, raising the possibility that cytokines produced by microglia induce molecular changes in Purkinje and granule neurons in AT (Figures 4A-B). Consistently, receptor-ligand analysis revealed increased cytokine signaling (*IL1B, IL7, IL4, IL34, IL15*) from microglia to granule and Purkinje neurons in AT (Figure S4).

**Dysregulated calcium signaling in AT**

GO analysis of genes downregulated in AT revealed significant enrichment of calcium related pathways (calcium ion transport, regulation of cytosolic calcium ion concentration, cellular calcium ion homeostasis) in AT Purkinje cells (Figure 4A, Figure S3B, Table S8). Among these genes was *ITPR1,* an endoplasmic reticulum (ER) calcium channel that causes spinocerebellar ataxias in an autosomal dominant manner[27,28] (Figure 4A). We asked whether additional cerebellar disease genes are differentially expressed in AT. Strikingly, hereditary ataxia genes with enriched expression in Purkinje cells (i.e., *KCNC3, PRKCG, ITPR1, KCND3, CACNA1G)* showed significant downregulation in AT Purkinje cells (Figure S5A). These disease genes were also enriched for calcium processes (calcium ion transport and regulation of cytosolic calcium ion concentration) (Figure S5B). These results suggest that *ATM* could be an upstream activator of calcium signaling and points to converging underlying mechanisms of a subset of hereditary ataxias in Purkinje cells. *HDAC4* is a known negative regulator of calcium ion genes (*ITPR1, DAB1)*[29], and *ATM* is an inhibitor of *HDAC4*[30]. Loss of *ATM* leads to nuclear accumulation of HDAC4, which could lead to dysregulated expression of *HDAC4* target genes. In support of this, we found significant overlap between *HDAC4* targets and AT downregulated genes (p-value 6.08e-22,

Fisher's exact test, Figure S5C). Taken together, these findings support that abnormal calcium ion homeostasis may be a direct consequence of *ATM* loss of function in Purkinje neurons, which may lead to aberrant firing patterns and ataxic phenotypes[31,32].

**Transcriptional dysregulation across cortical cell types in AT**

While AT is primarily known as a cerebellar degenerative disease, pathology in the cerebral cortex has been described, such as vascular changes and white matter scarring[33]. To compare the impact of *ATM* deficiency on the two brain regions, we next analyzed our snRNA-seq data from AT PFC. We used SingleR to annotate PFC cell types in an unbiased manner using an existing human PFC snRNA-seq dataset as a reference[13,34]. There were fifteen cell types identified, including astrocytes, microglia, endothelial cells, oligodendrocytes, OPCs, and multiple subtypes of excitatory and inhibitory neurons (Figure 5A). We next performed Dirichlet multinomial modeling to assess cell type proportion changes in AT PFC as done in the AT cerebellum analysis. As expected, there were no changes in the proportions of neuronal populations. However, oligodendrocytes were significantly decreased in AT PFC compared to control (Figure 5B), consistent with reports of cortical white matter degeneration in AT[33,35].

To characterize the biological pathways altered in AT PFC, we performed differential gene expression analysis followed by GO analysis for each cell type as previously described (Figure 5C, Figures S6A-B, Tables S9-S11). Overall, the number of DEGs and strength of gene expression changes in AT PFC was like those in AT CB (Figure 5C). Like AT cerebellar microglia, AT PFC microglia showed significant upregulation of innate and adaptive immune response pathways, including cytokine production involved in immune response, leukocyte cell-cell adhesion, and positive regulation of T cell proliferation (Figure 5D), suggesting similar disease mechanisms occurring in both brain regions. AT PFC also showed broad downregulation of metabolic pathways (oxidative phosphorylation, ATP biosynthetic process) and synaptic processes across cell types (Figure S6B, Table S11). Notably, myelination genes (*MAG, MBP, MYRF, PLLP)* were significantly downregulated in PFC oligodendrocytes in AT, demonstrating not only the loss but also the dysfunction of oligodendrocytes in AT PFC (Figure 5E). Taken together, these results demonstrate PFC specific dysregulation of oligodendrocytes in AT and shared activation of microglia in AT PFC and CB.

**Microglia are strongly and widely activated in AT cerebellum**

To systematically compare gene expression changes in AT cerebellum with AT PFC, we identified genes and pathways that are more significantly changed in AT cerebellum than AT PFC in common cell types between the two brain regions (microglia, OPC, oligodendrocytes, astrocytes, endothelial cells) (Figure S7, Tables S12-S14). While both cerebellar and cortical microglia showed upregulation of inflammatory pathways in AT, the microglia were more strongly activated in the cerebellum compared

to the PFC. Cerebellar AT microglia had significantly higher upregulation of genes related to inflammatory processes (leukocyte proliferation, adaptive immune response, macrophage migration) and neuronal death than AT PFC microglia (Figure 6A). Endothelial cells showed the most enrichment of downregulated pathways in AT cerebellum relative to PFC, including cell junction assembly, VEGF receptor signaling pathway, and establishment of endothelial barrier, suggesting that AT is associated with vascular dysfunction particularly in the cerebellum (Figure 6B).

Activated microglia associate with sites of injury and pathological changes across various neurodegenerative diseases[36] and can induce local neurodegeneration by phagocytosis of synapses and secretion of neurotoxic cytokines[37]. We thus sought to characterize the spatial distribution and number of microglia in AT and control cerebellum by immunostaining with the microglia marker CD11B. CD11B is a well-known marker of activated microglia in neurodegenerative inflammation[38]. In AT cerebellum, there were increased CD11B+ cells throughout the white matter, granule layer, and molecular layer compared to control cerebellum (Figure 6C). Across all layers, the number of CD11B+ microglia per area was significantly higher in AT compared to control (Bonferroni adjusted p-values < 1e-04, Mann-Whitney U test) (Figure 6C). These data confirm that AT cerebellum has a widespread increased presence of activated microglia.

**Activated microglia in AT cerebellum are transcriptionally similar to aging and neurodegeneration-associated microglia**

Our differential gene expression analysis indicated that microglia in AT cerebellum express activation markers, including strong upregulation of the complement genes, *C1QA, C1QB, C1QC,* and *C3* (Figure 7A). Increased expression of complement components is associated with microglial activation in neurodegenerative diseases such as Alzheimer's disease (AD)[39], where they have been shown to mediate synaptic loss and dysfunction[40,41]. To assess whether AT cerebellar microglia share additional features associated with microglia in aging and other neurodegenerative disorders, we compared the upregulated genes in AT cerebellar microglia with three gene sets: markers of aged human microglia, AD associated microglia markers from a human snRNA-seq study of AD, and markers of disease associated microglia (DAM) from a murine model of AD[11,42,43]. We found significant overlaps between AT cerebellar microglia upregulated genes and these three gene sets with the highest overlap with aging microglia (Fisher's exact test p-values < 1e-13; Figure 7B-C). *TREM2, TSPO, MS4A6A,* complement components, and MHC class II genes were among the overlapping genes, which have been associated with neuroinflammation and microglia activation[44] (Figure 7C). GO enrichment analysis of the overlapping genes and AT microglia specific upregulated genes revealed common enrichment in immune response and RNA processing related pathways, and AT specific enrichment of cytoskeletal

organization, ER stress, and regulation of neuron projection development (Figure 7D). Overall, these data show that AT cerebellar microglia share transcriptomic signatures found in aging and other neurodegenerative diseases.

## Microglia activation precedes Purkinje and granule cell death in disease progression

Microglia can be activated by a cell-intrinsic mechanism or in response to environmental cues such as neuronal death. To distinguish between these possibilities of AT microglia activation, we sought to determine when cerebellar microglia become activated in disease progression relative to Purkinje and granule cell death. We employed pseudotime analysis to understand the cell-type-specific cascades of molecular events across disease progression in AT [45]. For each cell type, cells were ordered along a continuous trajectory that progressed from the control to diseased state (Figure 8A). We performed differential analysis to identify genes that change as a function of pseudotime and clustered these genes by their pseudotime expression patterns. We then applied GO analysis to determine the enriched biological functions of each gene cluster. For microglia, the beginning of pseudotime (healthy state) had high expression of genes involved in cellular respiration, oxidative phosphorylation, and synaptic vesicle exocytosis, consistent with a high metabolism gene expression profile characteristic of cerebellar microglia[46] (Figure 8B). Over disease progression, upregulation of DNA repair genes (i.e., *XPA, RIF1, HLTF)* and CGAS-STING pathway genes (*CGAS, TRIM38, TRIM56*) was followed by leukocyte activation, cytokine production, and innate immune response. Lastly, genes involved in response to unfolded protein and defense response were strongly upregulated at the end of pseudotime, suggesting that ER stress occurs late in disease progression in microglia. In Purkinje neurons, disease progression was characterized first by a decline in genes related to calcium ion homeostasis (i.e., *ITPR1)* and cerebellum development*,* followed by upregulation in ribosome biogenesis and a cluster of genes related to ER stress (*HSPB1, XBP1)*, response to cytokine (*B2M, ISG15)*, and apoptotic signaling pathway (*BCL2, CASP3)* (Figure 8C). Granule neurons first demonstrated a decrease in neuron projection development and chromatin organization genes, followed by an increase in cellular respiration genes and genes related to response to cytokine, response to unfolded protein, and programmed cell death, suggesting that synaptic and metabolic dysfunction precedes granule neuron death in AT (Figure 8D).

We then compared molecular events between microglia, Purkinje, and granule cells along disease progression by aligning their pseudotime trajectories using dynamic time warping[47]. We compared the expression of inflammatory, calcium ion homeostasis, ER stress, and apoptotic genes over aligned pseudotime in the three cell types. The upregulation of complement (*C1QA, C1QB, C3),* and HLA genes in microglia coincides with downregulation of *ITPR1* in Purkinje cells (Figure 8E). Moreover, the microglia

inflammatory response and cytokine production (*CLEC7A, IL18, ROCK1, STAT3, complement, HLAs)* precedes the onset of response to cytokine (*HLAs, ARF1, B2M, UBA52)*, ER stress, and apoptosis genes (*TXNIP, XBP1, MUC1, BCL2)* in Purkinje and granule cells (Figure 8E). These findings suggest that microglial activation and inflammation precedes, and potentially induces, Purkinje and granule cell death in AT.

**Upregulation of the CGAS-STING pathway in AT microglia**

Microglia can be activated by neuronal death, a mechanism common to multiple neurodegenerative conditions[48]. However, since PFC neurons do not degenerate in AT and AT microglia are activated early in disease progression, we hypothesized that AT microglia in the PFC and cerebellum are cell-intrinsically activated. One potential mechanism of intrinsic activation is the accumulation of DNA damage due to *ATM* deficiency. Deficits in DNA repair caused by *ATM* deficiency are associated with increased cytosolic DNA[49]. Cytosolic DNA is recognized by the CGAS-STING pathway, which triggers an innate immune response by inducing type I interferons and inflammatory cytokines[50]. We found that genes within the CGAS-STING pathway, including *CGAS* and activators of CGAS signaling—*TRIM14, TRIM38,* and *TRIM56*[51–53]—were upregulated specifically in AT microglia from the cerebellum and PFC, suggesting the presence of cytosolic DNA ( Figure S8A). Moreover, upregulation of CGAS-STING genes was more prominent in cerebellar microglia (Figures S8A-B, FDR <0.05). These CGAS-STING pathway genes (*TRIM14, TRIM38, IFI16, IRF7*) were also upregulated in aged human microglia but not AD or DAM gene sets, implicating DNA damage and cytoplasmic DNA as a common underlying cause of microglial activation in AT and aging microglia, while AD microglia may be activated by another mechanism such as extrinsic stimuli (Table S15). Taken together, activation of the CGAS-STING pathway, potentially by self-chromatin fragments from deficits in DNA repair, suggests that cytosolic DNA contributes to microglial activation that is more pronounced in AT cerebellum than PFC.

Self-DNA enters the cytosol in a mitosis dependent manner, through the formation and rupture of DNA-damage induced micronuclei[54,55]. Thus, we hypothesized that underlying differences in proliferation may explain the differential activation of CGAS-STING in cerebellar microglia compared to PFC microglia. We tested whether microglia in the cerebellum and PFC differ in proliferation rate by inferring the cell cycle status of each cell by the expression of canonical markers of G1, S, and G2 phases. We found that cerebellar microglia have an increased percentage of cells in replicating phases compared to cortical microglia (p-value < 0.01, t-test) (Figure S8C). This is consistent with previous reports that cerebellar microglia have a higher turnover rate than cortical microglia, which may make them more vulnerable to accumulation of DNA damage due to *ATM* deficiency[56,57]. The differences in proliferation may underlie our observation that cerebellar microglia have a stronger CGAS-STING mediated immune

response in AT than cortical microglia. Overall, these findings support a model of AT disease pathogenesis in which early microglial activation due to genomic instability leads to Purkinje and granule cell death in AT (Figure S8D).

## Discussion

In this study, we present an atlas of human cerebellar transcriptomes in health and degeneration at single-cell resolution. We identified major neuronal and glial cell types in the cerebellum and recovered known and novel patterns of neurodegeneration in AT. We resolved cell-type-specific transcriptional perturbations in AT, including the activation of inflammatory pathways in microglia and the downregulation of calcium ion homeostasis pathways in Purkinje neurons. We found that hereditary ataxia genes have enriched expression in Purkinje neurons and converged on calcium ion homeostasis pathways. In addition, these genes were also significantly downregulated in AT, suggesting that *ATM* is upstream in a pathway that regulates the expression of calcium ion homeostasis genes.

Additionally, our findings reveal a pronounced activation of microglia in AT. We found striking enrichment of innate and adaptive immune response pathways among genes upregulated in AT microglia from both the cerebellum and PFC, however these genes were more significantly increased in AT cerebellar microglia. Neuropathological reports described cerebellar atrophy and unremarkable cortices across AT cases. The activation of microglia in AT PFC despite lack of cortical atrophy suggests that AT microglia are activated by a cell-intrinsic mechanism, with brain region specific factors leading to stronger activation in the cerebellum. We found that CGAS-STING pathway genes, including *CGAS* itself, were significantly upregulated specifically in AT microglia, with preferential activation in the cerebellum. The CGAS-STING pathway is activated in response to cytosolic DNA, suggesting the presence of cytosolic DNA in AT microglia. These results are consistent with recent reports of cytosolic DNA and CGAS-STING activation in microglia from mouse models of AT[10]. Potential sources of cytosolic DNA include release of nuclear self-DNA [49,50], mitochondrial DNA released by defective mitochondria[14,58,59], reverse-transcribed transposable elements as observed in aging-related disorders[60], and phagocytosis of nucleic acids from cellular debris. It will be of great interest for future work to identify the source of cytosolic DNA in AT microglia, as it is a novel potential therapeutic avenue for modulating inflammation in AT.

Activated microglia have been intensely studied in the context of neurodegenerative disorders including Alzheimer's disease, Parkinson's disease, and ALS[61]. Our study highlights the involvement of microglia in human cerebellar degeneration as well. Through pseudotime analyses, we found that the rise in inflammatory genes in AT microglia precedes the onset of ER stress, cytokine response, and apoptosis genes in AT Purkinje and granule neurons. These findings support a model of pathogenesis whereby cell-intrinsically activated microglia release neurotoxic

cytokines and factors that trigger Purkinje and granule cell death (Figure S8D). The presence of activated microglia in AT PFC without cortical neuron loss suggests that cerebellar Purkinje and granule neurons are more vulnerable to activated microglia. It is possible that cell autonomous and non-cell autonomous effects of *ATM* loss in cerebellar neurons and microglia interact to cause AT pathology. It will be important for future work to further dissect the developmental onset and contribution of cell type interactions to cerebellar degeneration in AT.

This study identifies cell-type-specific changes in AT across multiple brain regions and serves as a resource as the first large-scale adult human cerebellum dataset in health and degeneration. While granule and Purkinje neurons have been the most studied cell types in AT due to their selective degeneration, this study highlights the central role of microglia in AT cerebellar degenerative pathogenesis.

## Methods

### Isolation of single nuclei from fresh frozen tissue samples

All human postmortem brain tissue samples were obtained from the NIH NeuroBioBank. Samples were matched as closely as possible for age, sex, RIN, and PMI. All available neuropathology reports and medical records for each sample were obtained. Detailed sample information is in Table S1.

Nuclei isolation protocol was adapted from two previous publications[62,63]. All procedures were performed on ice or at 4°C. Fresh frozen samples were processed using a Dounce homogenizer in 5 ml of tissue lysis buffer (0.32M sucrose, 5mM $CaCl_2$, 3mM $MgAc_2$, 0.1mM EDTA, 10mM Tris-HCl (pH 8), 0.1% Triton X-100, 1mM DTT). The homogenized solution was loaded on top of a sucrose cushion (1.8M sucrose, 3mM $MgAc_2$, 10mM Tris-HCl (pH 8), 1mM DTT) and spun in an ultracentrifuge in an SW28 rotor (13,300 RPM, 2hrs, 4°c) to separate nuclei. After spinning, supernatant was removed and nuclei were resuspended (1% BSA in PBS plus 25ul 40U/ul RNAse inhibitor) then filtered through a 40um cell strainer. After filtration, nuclei were counted and diluted to a concentration of 1000 cells/ul.

### Droplet-based snRNA-seq

Droplet-based libraries were generated using the Chromium Single Cell 3’ v3 reagent kits (10x Genomics) according to manufacturer’s instructions. Resulting libraries were sequenced on an Illumina Novaseq at 150 paired-end reads.

### snRNA-seq analysis

snRNA-seq data for each individual was preprocessed and aligned to the GRCh38-3.0.0 reference genome using CellRanger count. After alignment, ambient/background RNA was removed from the count matrix using CellBender remove-background

(v0.2.0)[19]. The resulting count matrices were used to create Seurat objects per individual using Seurat v3[17]. Further quality control removed cells with less than 200 genes per cell, greater than 5000 genes per cell, and greater than 30% mitochondrial content. DoubletFinder[18] was used to detect and remove doublets with an expected multiplet rate of 7.6% for ~16,000 cells loaded per sample based on the 10x user guide.

SCTransform was used to perform normalization of expression values per sample[64]. After normalization, samples were integrated to align common clusters across individual datasets using Seurat's integration method[17]. Dimensionality reduction was performed using RunPCA and RunUMAP. A shared nearest neighbor graph was constructed using FindNeighbors with dims 1:30, k.param 100, and cosine metric. Clusters were then identified using the Leiden algorithm at a resolution of 1.5.

Marker genes for each cluster were obtained using FindAllMarkers with a minimum log2 fold-change of 0.25. Cluster markers were used to assign cerebellar cell type identities based on known literature cell type markers. For annotating clusters in the prefrontal cortex, SingleR was used for reference-based annotation since reference datasets from the human prefrontal cortex are available[34]. Velmeshev et al., 2019 was used as the prefrontal cortex reference[13].

To identify changes in cell type proportions in AT compared to controls, we used a Bayesian statistics approach to compositional data analysis previously described in the context of microbial ecology[20]. Compositional data has a negative covariance structure that is accounted for by the multinomial and Dirichlet probability distributions. We implemented Dirichlet multinomial modeling (DMM) using Hamiltonian Monte Carlo (HMC) using the R packages rstan and bayestestR (Stan Development Team (2020). "RStan: the R interface to Stan." R package version 2.21.2, http://mc-stan.org/.)[65]. The input to the model was a matrix of counts where the rows correspond to replicates (individual samples) and the columns correspond to cell types. We then modeled the replicates using the multinomial distribution for the probability of each cell type per individual. The Dirichlet distribution was used to model the multinomial parameters. The prior on the Dirichlet parameters was another Dirichlet distribution with a fixed parameter alpha $10^{-7}$, which gives uniform cell type proportions in expectation. The resulting posterior distributions were Dirichlet distributions of the cell type proportions in AT and control. We then subtracted the posterior probability distribution (89% credible interval) of control from AT to see whether there are significant differences in relative cell type composition. A cell type shift in log2 abundance ratio (AT/control) was considered significant if the 89% credible did not include 0.

**Differential gene expression and Gene Ontology analysis**

Differential gene expression analysis was performed on each cell type using edgeR[66]. The integrated Seurat object was subsetted to obtain Seurat objects for each cell type. The read counts were modeled and normalized using a negative binomial distribution with the trimmed mean of M-values (TMM) normalization method. To ensure robust signals, only genes that were expressed in at least 5% of one cell type were included in the analysis. The design matrix formula was ~ disease.status + sex + age + cellular detection rate. Differentially expressed genes between AT and control were identified using the likelihood ratio test (glmLRT). Genes with FDR < 0.05 and a log2 fold-change greater than 0.50 were used for downstream analysis.

Pseudobulk differential gene expression analysis was performed using DESeq2[67]. To generate pseudobulk data, we took the sum of raw counts for each gene over all cells in each sample, resulting in a gene by sample counts matrix. The design matrix was specified as ~ sex + age + disease.status. Differentially expressed genes between AT and controls were identified after running lfcShrink. Genes with FDR < 0.05 were considered statistically significant.

Gene Ontology (GO) enrichment analysis was performed on the upregulated and downregulated differentially expressed genes in each cell type using clusterProfiler[68]. GO biological processes with FDR < 0.05 were considered significant.

CellChat[69] was used to perform receptor-ligand analysis in order to identify differential cell-cell communication in AT compared to control. Differentially active signaling pathways with FDR<0.05 were considered significant.

**Module scores**

For select gene sets, module scores were calculated using AddModuleScore in Seurat. AddModuleScore calculates the average expression of a gene set in each cell, subtracted by the average expression of a control gene set, as previously described[70]. A positive score means the module of genes is expressed more highly in a particular cell than expected by chance. Cell cycle phase scores were similarly calculated based on canonical cell cycle markers using the Seurat function CellCycleScoring, which then outputs the predicted classification (G1, S, or G2M phase) for each cell.

**Disease gene analysis**

Known monogenic cerebellar disease genes were obtained from the Online Mendelian Inheritance in Man (OMIM) database. The mouse cerebellum data was obtained from Saunders et al., 2018[22]. To determine the correlation of cerebellar disease gene expression between humans and mice, cosine similarity was calculated between the human and mouse expression vectors of the genes for each cell type.

**Pseudotime analysis**

Pseudotime trajectory analysis was performed using Monocle2[45]. First, Seurat objects for each cell type (Microglia, Purkinje, and granule cells) were converted into the Monocle2 compatible cell dataset form using as.CellDataSet. Cells were clustered in an unsupervised manner using clusterCells. The top 1000 differentially expressed genes between AT and control in each cell type were used as the ordering genes to order cells along the pseudotime trajectory. The root state of the trajectory was defined as the cluster with the highest proportion of control cells. Genes that change as a function of pseudotime were identified using differentialGeneTest with the model formula specified as ~sm.ns(Pseudotime), which fits a natural spline to model gene expression as a smooth nonlinear function of pseudotime. Genes that change over pseudotime with an FDR < 0.05 were considered significant. These genes were then clustered according to their pseudotime expression profiles. GO enrichment analysis was performed on each cluster using clusterProfiler to identify the biological processes that co-vary across pseudotime.

To align the pseudotime trajectories between cell types, the method dynamic time warping (DTW) was applied as previously described[47]. DTW aligns similar temporal processes that differ in length by calculating the optimal matching between points in each sequence. For each cell type, ordered cells in pseudotime were binned into 100 “pseudocells” and the average expression of each gene was calculated within each pseudocell. The resulting gene x pseudocell matrices were the input for the dtw package in R. The Purkinje cell matrix was set as the reference and the other cell type was the query. The cost matrix was calculated as 1-corr(M1, M2), where corr(M1, M2) is the cosine similarity matrix between cell type 1 matrix (M1, reference) and cell type 2 matrix (M2, query). The query cell type pseudotime values were then warped into the reference to obtain aligned pseudotimes.

**Variant Calling**

Variant calling was performed on bam files containing all reads from all cells for each individual (“pseudobulk”) using bcftools mpileup and bcftools call. The variants for two cases were verified by whole genome sequencing.

**Immunostaining and Imaging**

Postmortem human formalin fixed vermis samples from four subjects diagnosed with Ataxia Telangiectasia and three age matched controls were obtained from the University of Maryland Brain and Tissue Bank. The samples were embedded in paraffin by the UMCCTS Biospecimen, Tissue and Tumor Bank, and sectioned on a LEICA RM2125 microtome. Sections were cut at 20 um thickness, placed on uncharged

untreated Fisherfinest premium microscope slides (product number 12-544-7), and dried overnight at 37°C. Eight sections (four control and four with AT pathology) were selected at random, deparaffinized with xylene and rehydrated in a graded ethanol wash series. This was followed by antigen retrieval, done by heating citrate buffer (pH 6.2) to 90°C and leaving the slides to soak for 45 minutes, then allowing the solution and slides to cool to room temperature. The samples were then subjected to brief PBS washes before application of a primary antibody solution consisting of blocking solution, 10% triton in 10x PBS for permeabilization, and primary antibody. Primary antibodies used included CD11B/Integrin Alpha M Monoclonal Antibody (Proteintech, product number 66519-1-Ig, concentration 1:100), and Anti-GFAP antibody produced in rabbit (Millipore Sigma product number HPA056030, concentration 1:250). The samples were incubated at 4°C overnight. The following day the samples were washed for an hour and a half in cold 1x PBS before application of secondary antibody solution consisting of blocking solution, 10% triton, and Donkey anti-Mouse Cross-Adsorbed Secondary Antibody, Alexa Fluor plus 555 (ThermoFisher Scientific, Invitrogen, product number A32773, concentration 1:125) and Donkey anti-Rabbit Cross-Adsorbed Secondary Antibody Alexa Fluor plus 488 (ThermoFisher Scientific, Invitrogen, product number A32790, concentration 1:125). After incubating overnight in the dark at 4°C the samples were washed in 1x PBS for an hour and a half in the dark. The tissue was stained for DAPI (ThermoFisher Scientific, Product Number 62248, concentration 1:10,000 in 1x PBS), washed and then treated with TrueBlack lipofuscin autofluorescence quencher (Biotium, product number 23007) according to the manufacturer's protocol. The samples were subjected to 30 minutes of washes in Barnstead water before being allowed to air dry. The tissue was mounted in Everbrite (Biotium, product number 23003) with Platinum Line cover glass (FisherScientific, Product Number 15-183-89) and left to cure overnight. Imaging was performed on a Zeiss LSM700 inverted microscope using ZEN Black 2012 Software.

**Statistics and reproducibility**

No statistical methods were used to predetermine sample sizes. All statistical tests were performed in R (v4.0.1) or Python (v3.8) with multiple hypothesis correction using the Benjamini-Hochberg procedure (FDR < 0.05) unless otherwise specified. Statistical tests are noted in figure legends, and include Fisher’s exact test, Student’s t-test and Mann-Whitney U-test.

**Data and Code availability**

The raw snRNA-seq data are available through the NCBI database of Genotypes and Phenotypes (dbGaP) with the accession number XXXXX. The processed datasets can be downloaded and explored through the interactive viewer on the Broad Single Cell

Portal at https://singlecell.broadinstitute.org/single_cell/study/SCP1300 and https://singlecell.broadinstitute.org/single_cell/study/SCP1302.

The code used to perform all analyses were adaptations from standard R packages as described in the Methods section.

**Author contributions**

E.A.L., M.A.L., J.K., and J.L. conceptualized the study. M.A.L., A.J., T.W.C., and P.G.B. performed single-nucleus RNA-sequencing experiments. J.L and J.K analyzed the single-nucleus RNA-sequencing data. A.T. performed the immunohistochemistry analyses. E.AL., T.W.Y, and M.A.L. supervised the study. J.L. wrote the manuscript. All authors reviewed and revised the manuscript.

**Acknowledgements**

We acknowledge the NIH NeuroBioBank for providing human tissues used in this study. We would like to thank Brad Margus from the AT Children's Project for helpful scientific discussion. We also acknowledge Allison R. McLean and Jeffery R. Gulcher from Genuity Sciences for their assistance with snRNA-seq data coordination. Illustrations were created with BioRender.com.

This work was supported by the National Institute of Health grants: K01 AG051791 (E.A.L), DP2 AG072437 (E.A.L), R00 AG054748 (M.A.L), AT Children's Project (E.A.L), Suh Kyungbae Foundation (E.A.L), Paul G. Allen Family Foundation (E.A.L), and Charles H. Hood Child Health Foundation (E.A.L., M.A.L). J.L. was supported by award T32GM007753 from the National Institute of General Medical Sciences. The content is solely the responsibility of the authors and does not necessarily represent the official views of the National Institute of General Medical Sciences or the National Institutes of Health.

**Figure Legends**

1. Single-nucleus RNA-sequencing of AT human cerebellum and prefrontal cortex.
    A. Schematic overview of experimental design and computational analyses.
    B. UMAP plot of major cell types identified in AT and control human cerebellum, downsampled to 10,000 cells for each condition.
    C. Top 5 marker genes for each major cell type in control cerebellum. Heatmap depicts centered and scaled log-normalized expression values.
    D. Cell type proportions in AT and control cerebellum.
    E. Relative abundance of cell types in AT versus control cerebellum, shown as the posterior distribution of Log2(proportion in AT/proportion in control) with 89% credible interval. Red bars highlight credible intervals that do not

overlap 0. Bolded cell type labels indicate a significant difference in relative abundance.

2. Monogenic cerebellar disease genes are expressed in specific cell types.
    A. Dotplot of average scaled expression of *ATM* in cell types of the adult human cerebellum and prefrontal cortex, and developing human cerebellum (Aldinger et al., 2021). Microglia have the highest expression of *ATM* out of all cell types in the cerebellum and PFC. Size of dot represents percentage of single cells expressing the gene. Expression scaled to mean of 0 and standard deviation of 1.
    B. Heatmap of cerebellar ataxia disease gene expression across cell types in human (left) and mouse (right) control cerebellum. Color represents centered and scaled log-normalized expression.
    C. Cosine similarity of human and mouse cell types based on expression of cerebellar ataxia disease genes.
3. Cell-type-specific transcriptional dysregulation in AT cerebellum.
    A. Differentially expressed genes (DEGs) in each cell type with FDR<0.05, |Log2FoldChange|>0.50. Each dot represents a significantly differentially expressed gene. Numbers of upregulated and downregulated DEGs per cell type are shown in red and blue text respectively.
    B. Fraction of single-nucleus up and down DEGs per cell type detected by pseudobulk analyses.
    C. Proportion of DEGs identified in different numbers of cell types.
    D. Proportion of cell-type-specific DEGs at increasing Log2FoldChange thresholds for DEG identification.
    E. Number of cell-type-specific up and down DEGs for each cell type.
4. Gene Ontology (GO) analysis of differentially expressed genes in AT cerebellum.
    A. Select enriched GO biological processes among DEGs in AT Purkinje neurons. Select genes in each pathway and their log2 fold-changes (AT/control) shown in the heatmap. Barplot shows significance of pathway enrichment.
    B. Select enriched GO biological processes among DEGs in AT granule neurons. Select genes in each pathway and their log2 fold-changes (AT/control) shown in the heatmap. Barplot shows significance of pathway enrichment.
    C. Select enriched GO biological processes among DEGs in AT CB microglia. Select genes in each pathway and their log2 fold-changes (AT/control) shown in the heatmap. Barplot shows significance of pathway enrichment.
5. Cell-type-specific transcriptional dysregulation in AT PFC.
    A. UMAP plot of major cell types in AT and control human PFC, downsampled to 10,000 cells per condition.

B. Relative abundance of cell types in AT versus control PFC, shown as the posterior distribution of Log2(proportion in AT/proportion in control) with 89% credible interval. Red bars highlight credible intervals that do not overlap 0. Bolded cell type labels indicate a significant difference in relative abundance.
C. Differentially expressed genes (DEGs) in each cell type with FDR<0.05, |Log2FoldChange|>0.50. Each dot represents a significantly differentially expressed gene.
D. Select enriched GO biological processes among DEGs in AT PFC microglia. Select genes in each pathway and their log2 fold-changes (AT/control) shown in the heatmap. Barplot shows significance of pathway enrichment.
E. Select enriched GO biological processes among DEGs in AT PFC oligodendrocytes. Violin plot of normalized expression of myelination genes *MAG*, *MBP*, *MYRF*, and *PLLP* in AT and control PFC oligodendrocytes.

6. Stronger activation of microglia in AT cerebellum compared to PFC.
   A. Heatmap showing enriched GO biological processes and log2 fold-changes of significant DEGs in each pathway with greater upregulation in AT CB microglia than AT PFC microglia.
   B. Heatmap showing enriched GO biological processes and log2 fold-changes of significant DEGs in each pathway with greater downregulation in AT CB endothelial cells than AT PFC endothelial cells.
   C. *CD11B* immunostaining of postmortem cerebellar cortex from AT and controls. Red: *CD11B.* Green: *GFAP*. Blue: DAPI. WM: white matter. GL: granule layer. ML: molecular layer. Quantification of *CD11B* immunostaining across cerebellar cortex layers in AT and control. ****Bonferroni-adjusted p-value<1e-04, Mann-Whitney U test.
7. AT cerebellar microglia upregulate markers of aging and neurodegenerative microglia.
   A. Average scaled expression of complement components *C1QA, C1QB, C1QC, C3* in microglia from AT and control cerebellum.
   B. Overlap between AT microglia (AT) upregulated genes and human Alzheimer's disease microglia markers (AD, Mathys et al., 2019), Disease Associated Microglia markers (DAM, Keren-Shaul et al., 2017), and human aging microglia markers (Aged, Olah et al., 2018). Overlap p-values from Fisher's exact test shown in each cell. Color represents -log10(overlap p-value). Number of genes in each set and intersection shown in parentheses.

C. Heatmap of AT microglia log2 fold-changes (FDR<0.05) for overlapping microglia markers. AT_AD: AT and Alzheimer's disease microglia overlapping genes. AT_DAM: AT and DAM overlapping genes. AT_AGED: AT and human aging microglia overlapping genes.
D. GO biological process enrichment of overlapping microglia markers. AT: AT microglia only upregulated genes. Pathways with FDR<0.05 shown.

8. Pseudotime analysis of disease progression reveals early microglia activation.
   A. Disease progression pseudotime trajectory of AT cerebellar microglia, colored by disease status (red: AT, blue: control), or pseudotime (healthy to diseased).
   B. Heatmap of genes that significantly change over pseudotime in microglia, clustered by pseudotemporal expression patterns. Each cluster is annotated with enriched GO terms (FDR<0.05). Expression of *CD11B, CGAS, TRIM14, TRIM38,* and *TRIM56* over pseudotime in microglia.
   C. Heatmap of genes that change over pseudotime in Purkinje neurons, clustered by pseudotemporal expression patterns. Each cluster is annotated with enriched GO terms (FDR<0.05). Expression of *BCL6, CASP3, ITPR1,* and *XBP1* in Purkinje neurons over pseudotime.
   D. Heatmap of genes that change over pseudotime in granule neurons, clustered by pseudotemporal expression patterns. Each cluster is annotated with enriched GO terms (FDR<0.05). Heatmaps in b, c, d depict center and scaled expression.
   E. Expression of select genes over aligned pseudotime in microglia, Purkinje and granule neurons, showing a rise in inflammatory markers in microglia preceding the rise in ER stress and apoptotic markers in Purkinje and granule neurons.

**Supplemental Figure Legends**

Figure S1. Quality control data for snRNA-seq data from cerebellum and PFC.

A. Transcript (nCount_RNA), gene (nFeature_RNA), percent transcripts from mitochondrial genes, and percent transcripts from ribosomal genes per cerebellar sample before quality control filtering.
B. Transcript (nCount_RNA), gene (nFeature_RNA), percent transcripts from mitochondrial genes, and percent transcripts from ribosomal genes per cerebellar sample after quality control filtering.
C. UMAP plots of cerebellar data showing integration of samples, sex, age, and disease status.
D. Stacked barplots showing proportion of each cell type per cerebellar sample.

E. Posterior distribution of log2 ratio of cell type proportions in AT cerebellum after 500 random permutations.
F. Transcript (nCount_RNA), gene (nFeature_RNA), percent transcripts from mitochondrial genes, and percent transcripts from ribosomal genes per PFC sample before quality control filtering.
G. Transcript (nCount_RNA), gene (nFeature_RNA), percent transcripts from mitochondrial genes, and percent transcripts from ribosomal genes per PFC sample after quality control filtering.
H. UMAP plots of cerebellar data showing integration of samples, disease status, sex, and age.
I. Stacked barplots showing proportion of each cell type per PFC sample.
J. Posterior distribution of log2 ratio of cell type proportions in AT PFC after 500 random permutations.

Figure S2. Candidate pathogenic *ATM* variants in AT cases
Alignment tracks of whole genome sequencing (WGS) or snRNA-seq reads at the *ATM* locus showing pathogenic variants in AT cases. WGS data was aligned to reference hg19. snRNA-seq data was aligned to reference hg38.

Figure S3. Enrichment of upregulated and downregulated pathways across cell types in AT cerebellum.
A. Heatmap of enriched pathways among upregulated DEGs in cell types from AT cerebellum.
B. Heatmap of enriched pathways among downregulated DEGs in cell types from AT cerebellum. Color represents z-score of pathway significance.

Figure S4. Altered cell-cell communication in AT cerebellum.
A. Relative information flow for signaling pathways enriched in AT or control cerebellum. Information flow for each pathway is calculated as the sum of the communication probability among all pairs of cell groups.
B. Ligand-receptor pairs with increased communication probability between microglia, granule, and Purkinje neurons in AT cerebellum compared to control. Dot color represents communication probability (strength of signaling) and dot size represents significance of ligand-receptor pair. Empty space represents a communication probability of zero.

Figure S5. Dysregulation of hereditary ataxia genes in AT.
A. Heatmap showing log2 fold-change of hereditary ataxia genes in AT cerebellum. *FDR<0.05. *ATM* expression increased in several cell types in AT cerebellum,

suggesting that lack of ATM function induces compensatory increases in transcription of the *ATM* locus.

**B.** Enriched GO pathways among disease genes with enriched expression in Purkinje cells and downregulated in AT Purkinje cells.

C. Overlap between HDAC4 neuronal target genes and downregulated DEGs in AT cerebellum.

Figure S6. Enrichment of upregulated and downregulated pathways across cell types in AT PFC.

A. Heatmap of enriched pathways among upregulated DEGs in cell types from AT PFC.
B. Heatmap of enriched pathways among downregulated DEGs in cell types from AT PFC. Color represents z-score of pathway significance.

Figure S7. Enrichment of pathways with greater dysregulation in AT cerebellum than AT PFC.

A. Heatmap of enriched pathways among DEGs upregulated in AT CB v. AT PFC.
B. Heatmap of enriched pathways among DEGs downregulated in AT CB v. AT PFC. Color represents z-score of pathway significance.

Figure S8. Expression of CGAS-STING enriched in microglia from cerebellum and PFC.

A. Dotplot of average scaled expression of CGAS-STING pathway genes in cell types of the cerebellum and PFC in AT and control. Heatmap shows log2 fold-change of CGAS-STING pathway genes in AT cerebellar microglia versus AT PFC microglia. *FDR<0.05.
B. CGAS module scores in AT cerebellum and PFC versus controls. ***p-value<4e-16, Mann-Whitney U test.
C. Percentage of microglia putatively in replicating phase in control cerebellum and PFC. **p-value <0.01, t-test.
D. Schematic of mechanistic model of cerebellar degeneration in AT.

**Supplemental Table Legends**

I. Detailed Sample Information: ID, Diagnosis, Region, Batch, Age, Sex, PMI, RIN
II. Sample Summary Information
III. Neuropathology report and medical record summaries
IV. ATM mutations in AT cases
V. Cerebellar ataxia disease genes list and OMIM numbers
VI. Cerebellum significant DEGs per cell type
VII. AT CB up DEG GO enrichment
VIII. AT CB down DEG GO enrichment

IX. PFC significant DEGs per cell type
X. AT PFC up DEG GO enrichment
XI. AT PFC down DEG GO enrichment
XII. CB v. PFC significant DEGs per cell type
XIII. AT CB v. AT PFC up DEG GO enrichment
XIV. AT CB v. AT PFC down DEG GO enrichment
XV. Overlapping genes between AT microglia up DEGs and aging and neurodegenerative microglia markers

## References


1. Savitsky, K. *et al.* A single ataxia telangiectasia gene with a product similar to PI-3 kinase. *Science* **268**, 1749–1753 (1995).
2. Martin F. Lavin, K. K. K. Review: ATM: the protein encoded by the gene mutated in the radiosensitive syndrome ataxia-telangiectasia. *International Journal of Radiation Biology* **75**, 1201–1214 (1999).
3. Watters, D. *et al.* Cellular localisation of the ataxia-telangiectasia (ATM) gene product and discrimination between mutated and normal forms. *Oncogene* **14**, 1911–1921 (1997).
4. Zhang, Y. *et al.* Mitochondrial redox sensing by the kinase ATM maintains cellular antioxidant capacity. *Sci Signal* **11**, (2018).
5. Cheng, A. *et al.* ATM loss disrupts the autophagy-lysosomal pathway. *Autophagy* 1–13 (2020) doi:10.1080/15548627.2020.1805860.
6. Lavin, M. F. The appropriateness of the mouse model for ataxia-telangiectasia: Neurological defects but no neurodegeneration. *DNA Repair* **12**, 612–619 (2013).
7. Jiang, D. *et al.* Alteration in 5-hydroxymethylcytosine-mediated epigenetic regulation leads to Purkinje cell vulnerability in ATM deficiency. *Brain* **138**, 3520–3536 (2015).
8. Nayler, S. P. *et al.* Human iPSC-Derived Cerebellar Neurons from a Patient with Ataxia-Telangiectasia Reveal Disrupted Gene Regulatory Networks. *Front Cell Neurosci* **11**, 321 (2017).

9. Petersen, A. J., Rimkus, S. A. & Wassarman, D. A. ATM kinase inhibition in glial cells activates the innate immune response and causes neurodegeneration in Drosophila. *Proc. Natl. Acad. Sci. U.S.A.* **109**, E656-664 (2012).
10. Song, X., Ma, F. & Herrup, K. Accumulation of Cytoplasmic DNA Due to ATM Deficiency Activates the Microglial Viral Response System with Neurotoxic Consequences. *J Neurosci* **39**, 6378–6394 (2019).
11. Mathys, H. *et al.* Single-cell transcriptomic analysis of Alzheimer's disease. *Nature* **570**, 332–337 (2019).
12. Schirmer, L. *et al.* Neuronal vulnerability and multilineage diversity in multiple sclerosis. *Nature* **573**, 75–82 (2019).
13. Velmeshev, D. *et al.* Single-cell genomics identifies cell type–specific molecular changes in autism. *Science* **364**, 685 (2019).
14. Lee, H. *et al.* Cell Type-Specific Transcriptomics Reveals that Mutant Huntingtin Leads to Mitochondrial RNA Release and Neuronal Innate Immune Activation. *Neuron* **107**, 891-908.e8 (2020).
15. Nagy, C. *et al.* Single-nucleus transcriptomics of the prefrontal cortex in major depressive disorder implicates oligodendrocyte precursor cells and excitatory neurons. *Nature Neuroscience* **23**, 771–781 (2020).
16. Wallis, L. I. *et al.* Proton Spectroscopy and Imaging at 3T in Ataxia-Telangiectasia. *American Journal of Neuroradiology* **28**, 79–83 (2007).
17. Stuart, T. *et al.* Comprehensive Integration of Single-Cell Data. *Cell* **177**, 1888-1902.e21 (2019).
18. McGinnis, C. S., Murrow, L. M. & Gartner, Z. J. DoubletFinder: Doublet Detection in Single-Cell RNA Sequencing Data Using Artificial Nearest Neighbors. *Cell Syst* **8**, 329-337.e4 (2019).

19. Fleming, S. J., Marioni, J. C. & Babadi, M. CellBender remove-background: a deep generative model for unsupervised removal of background noise from scRNA-seq datasets. *bioRxiv* 791699 (2019) doi:10.1101/791699.
20. Harrison, J. G., Calder, W. J., Shastry, V. & Buerkle, C. A. Dirichlet-multinomial modelling outperforms alternatives for analysis of microbiome and other ecological count data. *Molecular Ecology Resources* **20**, 481–497 (2020).
21. Aldinger, K. A. *et al.* Spatial and cell type transcriptional landscape of human cerebellar development. *Nat Neurosci* 1–13 (2021) doi:10.1038/s41593-021-00872-y.
22. Saunders, A. *et al.* Molecular Diversity and Specializations among the Cells of the Adult Mouse Brain. *Cell* **174**, 1015-1030.e16 (2018).
23. Becherel, O. J. *et al.* Senataxin Plays an Essential Role with DNA Damage Response Proteins in Meiotic Recombination and Gene Silencing. *PLoS Genet* **9**, (2013).
24. Ugur, B., Hancock-Cerutti, W., Leonzino, M. & De Camilli, P. Role of VPS13, a protein with similarity to ATG2, in physiology and disease. *Current Opinion in Genetics & Development* **65**, 61–68 (2020).
25. Ximerakis, M. *et al.* Single-cell transcriptomic profiling of the aging mouse brain. *Nature Neuroscience* **22**, 1696–1708 (2019).
26. Zahn, J. M. *et al.* AGEMAP: A Gene Expression Database for Aging in Mice. *PLOS Genetics* **3**, e201 (2007).
27. van de Leemput, J. *et al.* Deletion at ITPR1 underlies ataxia in mice and spinocerebellar ataxia 15 in humans. *PLoS Genet* **3**, e108 (2007).
28. Huang, L. *et al.* Missense mutations in ITPR1 cause autosomal dominant congenital nonprogressive spinocerebellar ataxia. *Orphanet J Rare Dis* **7**, 67 (2012).
29. Sando, R. *et al.* HDAC4 Governs a Transcriptional Program Essential for Synaptic Plasticity and Memory. *Cell* **151**, 821–834 (2012).

30. Li, J. *et al.* Nuclear accumulation of HDAC4 in ATM deficiency promotes neurodegeneration in ataxia telangiectasia. *Nat. Med.* **18**, 783–790 (2012).
31. Hisatsune, C. *et al.* IP3R1 deficiency in the cerebellum/brainstem causes basal ganglia-independent dystonia by triggering tonic Purkinje cell firings in mice. *Front. Neural Circuits* **7**, (2013).
32. Hasan, G. & Sharma, A. Regulation of neuronal physiology by Ca2+ release through the IP3R. *Current Opinion in Physiology* **17**, 1–8 (2020).
33. Sahama, I. *et al.* Altered corticomotor-cerebellar integrity in young ataxia telangiectasia patients. *Mov Disord* **29**, 1289–1298 (2014).
34. Aran, D. *et al.* Reference-based analysis of lung single-cell sequencing reveals a transitional profibrotic macrophage. *Nature Immunology* **20**, 163–172 (2019).
35. Tse, K.-H. & Herrup, K. DNA damage in the oligodendrocyte lineage and its role in brain aging. *Mech Ageing Dev* **161**, 37–50 (2017).
36. Song, W. M. & Colonna, M. The identity and function of microglia in neurodegeneration. *Nature Immunology* **19**, 1048–1058 (2018).
37. Nakayama, H. *et al.* Microglia permit climbing fiber elimination by promoting GABAergic inhibition in the developing cerebellum. *Nature Communications* **9**, 2830 (2018).
38. Roy, A., Fung, Y. K., Liu, X. & Pahan, K. Up-regulation of Microglial CD11b Expression by Nitric Oxide. *J Biol Chem* **281**, 14971–14980 (2006).
39. Wu, T. *et al.* Complement C3 Is Activated in Human AD Brain and Is Required for Neurodegeneration in Mouse Models of Amyloidosis and Tauopathy. *Cell Reports* **28**, 2111-2123.e6 (2019).
40. Jafari, M. *et al.* Phagocyte-mediated synapse removal in cortical neuroinflammation is promoted by local calcium accumulation. *Nature Neuroscience* 1–13 (2021) doi:10.1038/s41593-020-00780-7.

41. Hong, S. *et al.* Complement and microglia mediate early synapse loss in Alzheimer mouse models. *Science* **352**, 712–716 (2016).
42. Olah, M. *et al.* A transcriptomic atlas of aged human microglia. *Nat Commun* **9**, (2018).
43. Keren-Shaul, H. *et al.* A Unique Microglia Type Associated with Restricting Development of Alzheimer's Disease. *Cell* **169**, 1276-1290.e17 (2017).
44. Patir, A., Shih, B., McColl, B. W. & Freeman, T. C. A core transcriptional signature of human microglia: Derivation and utility in describing region-dependent alterations associated with Alzheimer's disease. *Glia* **67**, 1240–1253 (2019).
45. Qiu, X. *et al.* Reversed graph embedding resolves complex single-cell trajectories. *Nature Methods* **14**, 979–982 (2017).
46. Grabert, K. *et al.* Microglial brain region-dependent diversity and selective regional sensitivities to aging. *Nat Neurosci* **19**, 504–516 (2016).
47. Cacchiarelli, D. *et al.* Aligning Single-Cell Developmental and Reprogramming Trajectories Identifies Molecular Determinants of Myogenic Reprogramming Outcome. *Cell Systems* **7**, 258-268.e3 (2018).
48. Marín-Teva, J. L., Cuadros, M. A., Martín-Oliva, D. & Navascués, J. Microglia and neuronal cell death. *Neuron Glia Biol* **7**, 25–40 (2011).
49. Härtlova, A. *et al.* DNA Damage Primes the Type I Interferon System via the Cytosolic DNA Sensor STING to Promote Anti-Microbial Innate Immunity. *Immunity* **42**, 332–343 (2015).
50. Dou, Z. *et al.* Cytoplasmic chromatin triggers inflammation in senescence and cancer. *Nature* **550**, 402–406 (2017).
51. Chen, M. *et al.* TRIM14 Inhibits cGAS Degradation Mediated by Selective Autophagy Receptor p62 to Promote Innate Immune Responses. *Mol Cell* **64**, 105–119 (2016).
52. Seo, G. J. *et al.* TRIM56-mediated monoubiquitination of cGAS for cytosolic DNA sensing. *Nature Communications* **9**, 613 (2018).

53. Hu, M.-M. & Shu, H.-B. Multifaceted roles of TRIM38 in innate immune and inflammatory responses. *Cell Mol Immunol* **14**, 331–338 (2017).

54. Harding, S. M. *et al.* Mitotic progression following DNA damage enables pattern recognition within micronuclei. *Nature* **548**, 466–470 (2017).

55. Mackenzie, K. J. *et al.* cGAS surveillance of micronuclei links genome instability to innate immunity. *Nature* **548**, 461–465 (2017).

56. Tay, T. L., Sagar, Dautzenberg, J., Grün, D. & Prinz, M. Unique microglia recovery population revealed by single-cell RNAseq following neurodegeneration. *Acta Neuropathologica Communications* **6**, 87 (2018).

57. Stowell, R. D. *et al.* Cerebellar microglia are dynamically unique and survey Purkinje neurons in vivo. *Dev Neurobiol* **78**, 627–644 (2018).

58. Dhir, A. *et al.* Mitochondrial double-stranded RNA triggers antiviral signalling in humans. *Nature* **560**, 238–242 (2018).

59. Sprenger, H.-G. *et al.* Cellular pyrimidine imbalance triggers mitochondrial DNA–dependent innate immunity. *Nature Metabolism* 1–15 (2021) doi:10.1038/s42255-021-00385-9.

60. De Cecco, M. *et al.* L1 drives IFN in senescent cells and promotes age-associated inflammation. *Nature* **566**, 73–78 (2019).

61. Hickman, S., Izzy, S., Sen, P., Morsett, L. & El Khoury, J. Microglia in neurodegeneration. *Nature Neuroscience* **21**, 1359–1369 (2018).

62. Matevossian, A. & Akbarian, S. Neuronal nuclei isolation from human postmortem brain tissue. *J Vis Exp* 914 (2008) doi:10.3791/914.

63. Spalding, K. L., Bhardwaj, R. D., Buchholz, B. A., Druid, H. & Frisén, J. Retrospective birth dating of cells in humans. *Cell* **122**, 133–143 (2005).

64. Hafemeister, C. & Satija, R. Normalization and variance stabilization of single-cell RNA-seq data using regularized negative binomial regression. *Genome Biology* **20**, 296 (2019).

65. Makowski, D., Ben-Shachar, M. S. & Lüdecke, D. bayestestR: Describing Effects and their Uncertainty, Existence and Significance within the Bayesian Framework. *Journal of Open Source Software* **4**, 1541 (2019).

66. McCarthy, D. J., Chen, Y. & Smyth, G. K. Differential expression analysis of multifactor RNA-Seq experiments with respect to biological variation. *Nucleic Acids Research* **40**, 4288–4297 (2012).

67. Love, M. I., Huber, W. & Anders, S. Moderated estimation of fold change and dispersion for RNA-seq data with DESeq2. *Genome Biology* **15**, 550 (2014).

68. Yu, G., Wang, L.-G., Han, Y. & He, Q.-Y. clusterProfiler: an R Package for Comparing Biological Themes Among Gene Clusters. *OMICS: A Journal of Integrative Biology* **16**, 284–287 (2012).

69. Jin, S. *et al.* Inference and analysis of cell-cell communication using CellChat. *Nat Commun* **12**, 1088 (2021).

70. Tirosh, I. *et al.* Dissecting the multicellular ecosystem of metastatic melanoma by single-cell RNA-seq. *Science* **352**, 189–196 (2016).

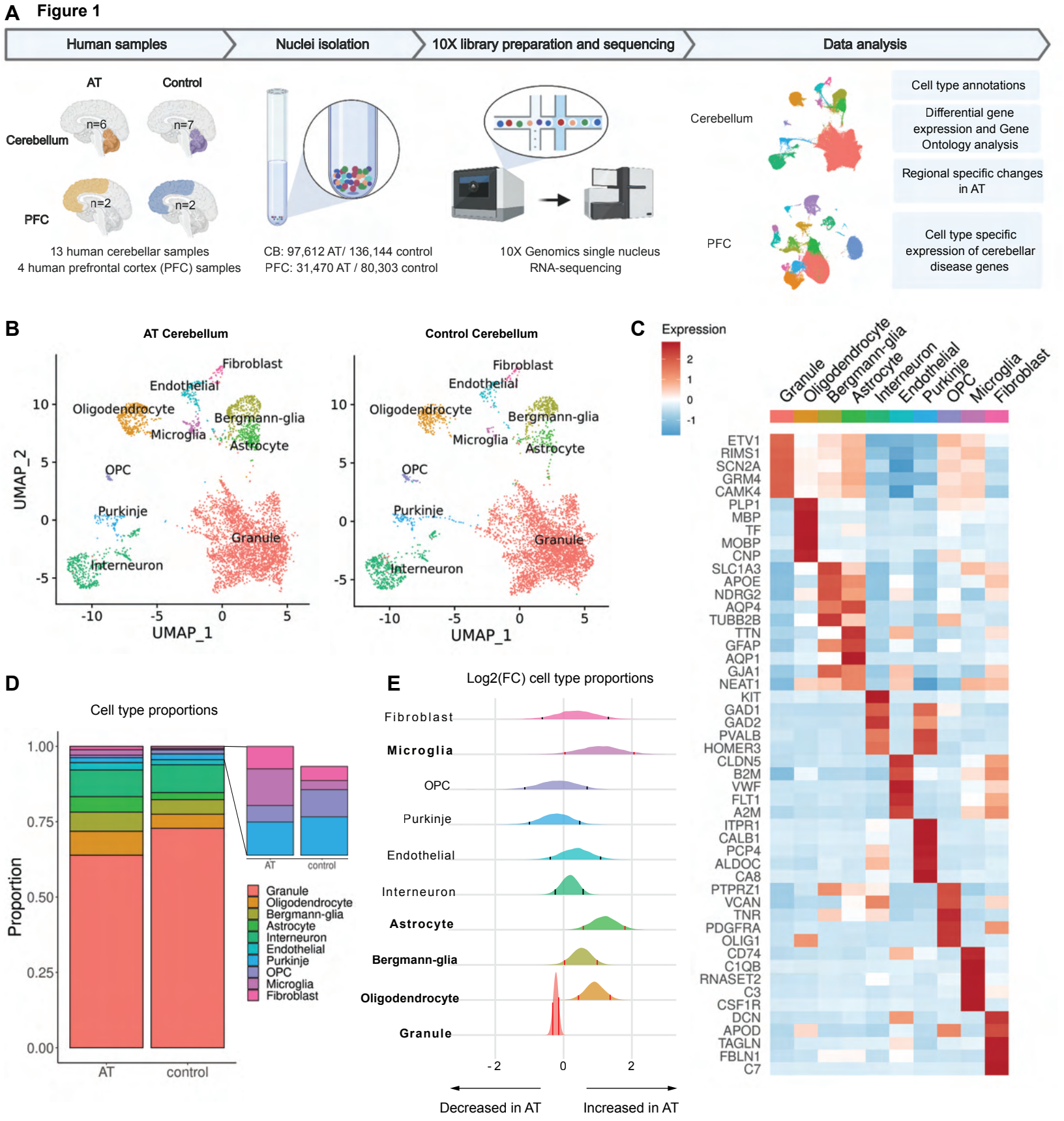


Figure 1. Single-nucleus RNA-sequencing of AT human cerebellum and prefrontal cortex.
A. Schematic overview of experimental design and computational analyses.
B. UMAP plot of major cell types identified in AT and control human cerebellum, downsampled to 10,000 cells for each condition.
C. Top 5 marker genes for each major cell type in control cerebellum. Heatmap depicts centered and scaled log-normalized expression values.
D. Cell type proportions in AT and control cerebellum.
E. Relative abundance of cell types in AT versus control cerebellum, shown as the posterior distribution of Log2(proportion in AT/ proportion in control) with 89% credible interval. Red bars highlight credible intervals that do not overlap 0. Bolded cell type labels indicate a significant difference in relative abundance.

**Figure 2**

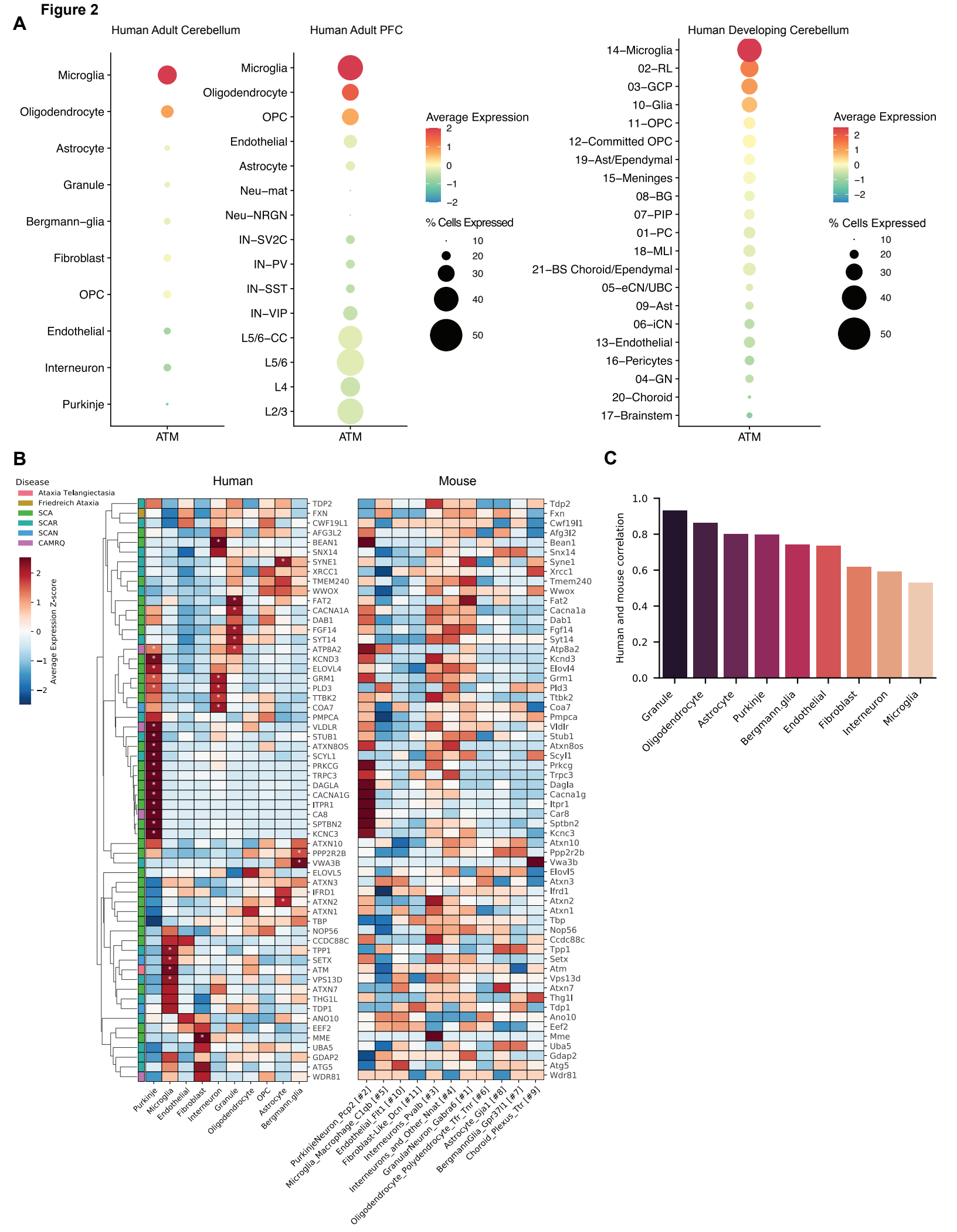
A
Human Adult Cerebellum
Microglia
Oligodendrocyte
Astrocyte
Granule
Bergmann–glia
Fibroblast
OPC
Endothelial
Interneuron
Purkinje
ATM
Human Adult PFC
Microglia
Oligodendrocyte
OPC
Endothelial
Astrocyte
Neu–mat
Neu–NRGN
IN–SV2C
IN–PV
IN–SST
IN–VIP
L5/6–CC
L5/6
L4
L2/3
ATM
Average Expression
2
1
0
−1
−2
% Cells Expressed
10
20
30
40
50
Human Developing Cerebellum
14–Microglia
02–RL
03–GCP
10–Glia
11–OPC
12–Committed OPC
19–Ast/Ependymal
15–Meninges
08–BG
07–PIP
01–PC
18–MLI
21–BS Choroid/Ependymal
05–eCN/UBC
09–Ast
06–iCN
13–Endothelial
16–Pericytes
04–GN
20–Choroid
17–Brainstem
ATM
Average Expression
2
1
0
−1
−2
% Cells Expressed
10
20
30
40
50
B
Disease
Ataxia Telangiectasia
Friedreich Ataxia
SCA
SCAR
SCAN
CAMRQ
Average Expression Z-score
2
1
0
−1
−2
Human
Mouse
TDP2
FXN
CWF19L1
AFG3L2
BEAN1
SNX14
SYNE1
XRCC1
TMEM240
WWOX
FAT2
CACNA1A
DAB1
FGF14
SYT14
ATP8A2
KCND3
ELOVL4
GRM1
PLD3
TTBK2
COA7
PMPCA
VLDLR
STUB1
ATXN8OS
SCYL1
PRKCG
TRPC3
DAGLA
CACNA1G
ITPR1
CA8
SPTBN2
KCNC3
ATXN10
PPP2R2B
VWA3B
ELOVL5
ATXN3
IFRD1
ATXN2
ATXN1
TBP
NOP56
CCDC88C
TPP1
SETX
ATM
VPS13D
ATXN7
THG1L
TDP1
ANO10
EEF2
MME
UBA5
GDAP2
ATG5
WDR81
Purkinje
Microglia
Endothelial
Fibroblast
Interneuron
Granule
Oligodendrocyte
OPC
Astrocyte
Bergmann.glia
Tdp2
Fxn
Cwf19l1
Afg3l2
Bean1
Snx14
Syne1
Xrcc1
Tmem240
Wwox
Fat2
Cacna1a
Dab1
Fgf14
Syt14
Atp8a2
Kcnd3
Elovl4
Grm1
Pld3
Ttbk2
Coa7
Pmpca
Vldlr
Stub1
Atxn8os
Scyl1
Prkcg
Trpc3
Dagla
Cacna1g
Itpr1
Car8
Sptbn2
Kcnc3
Atxn10
Ppp2r2b
Vwa3b
Elovl5
Atxn3
Ifrd1
Atxn2
Atxn1
Tbp
Nop56
Ccdc88c
Tpp1
Setx
Atm
Vps13d
Atxn7
Thg1l
Tdp1
Ano10
Eef2
Mme
Uba5
Gdap2
Atg5
Wdr81
PurkinjeNeuron_Pcp2 [#2]
Microglia_Macrophage_C1qb [#5]
Endothelial_Flt1 [#10]
Fibroblast-Like_Dcn [#11]
Interneurons_Pvalb [#3]
Interneurons_and_Other_Nnat [#4]
GranularNeuron_Gabra6 [#1]
Oligodendrocyte_Polydendrocyte_Tfr_Tnr [#6]
Astrocyte_Gja1 [#8]
BergmannGlia_Gpr37l1 [#7]
Choroid_Plexus_Ttr [#9]
C
Human and mouse correlation
1.0
0.8
0.6
0.4
0.2
0.0
Granule
Oligodendrocyte
Astrocyte
Purkinje
Bergmann.glia
Endothelial
Fibroblast
Interneuron
Microglia

Figure 2. Monogenic cerebellar disease genes are expressed in specific cell types.

A. Dotplot of average scaled expression of *ATM* in cell types of the adult human cerebellum and prefrontal cortex, and developing human cerebellum (Aldinger et al., 2021). Microglia have the highest expression of *ATM* out of all cell types in the cerebellum and PFC. Size of dot represents percentage of single cells expressing the gene. Expression scaled to mean of 0 and standard deviation of 1.
B. Heatmap of cerebellar ataxia disease gene expression across cell types in human (left) and mouse (right) control cerebellum. Color represents centered and scaled log-normalized expression.
C. Cosine similarity of human and mouse cell types based on expression of cerebellar ataxia disease genes.

Figure 3

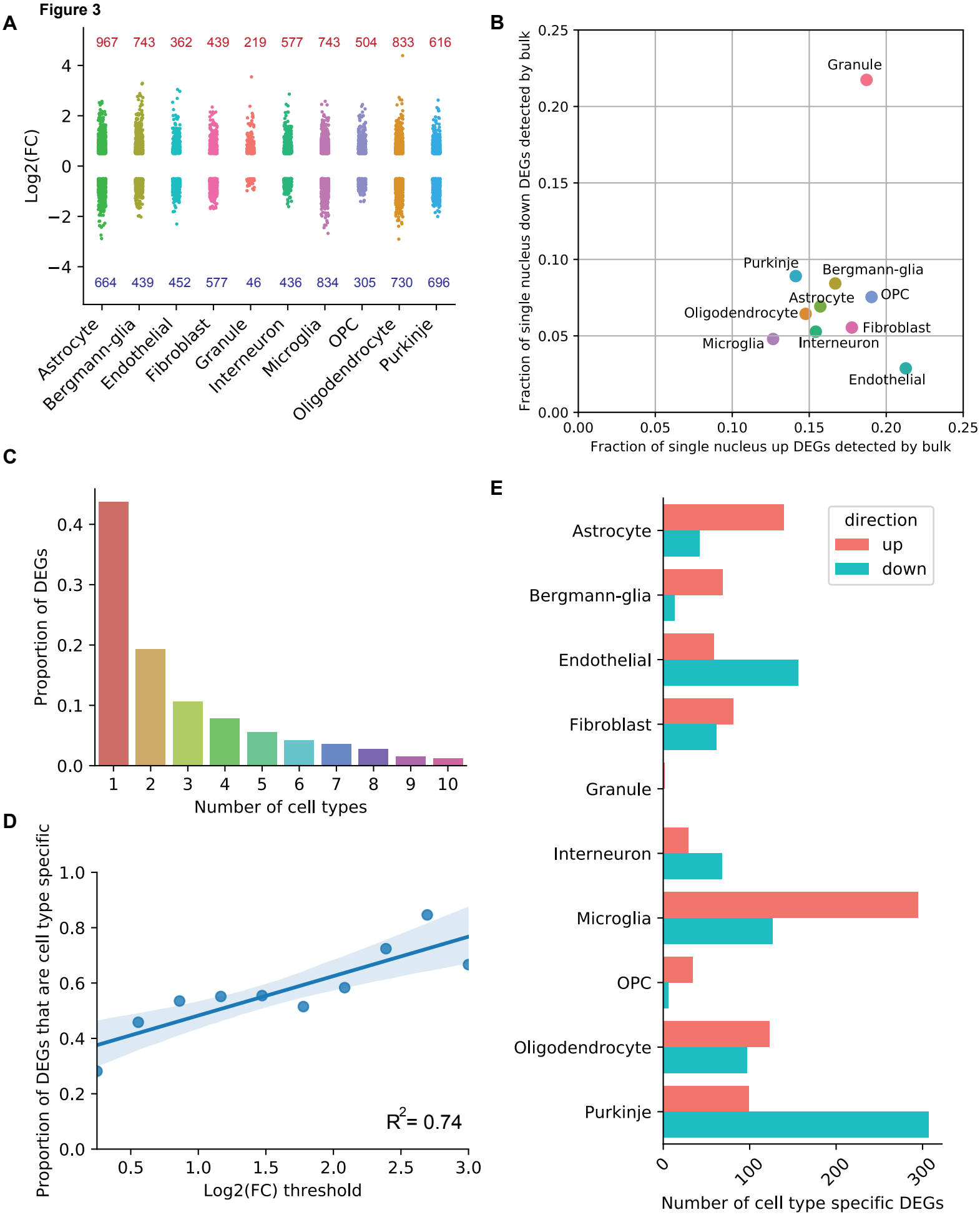
A
967 743 362 439 219 577 743 504 833 616
664 439 452 577 46 436 834 305 730 696
Log2(FC)
Astrocyte
Bergmann-glia
Endothelial
Fibroblast
Granule
Interneuron
Microglia
OPC
Oligodendrocyte
Purkinje
B
Fraction of single nucleus down DEGs detected by bulk
Fraction of single nucleus up DEGs detected by bulk
Granule
Purkinje
Bergmann-glia
Astrocyte
OPC
Oligodendrocyte
Fibroblast
Microglia
Interneuron
Endothelial
C
Proportion of DEGs
Number of cell types
D
Proportion of DEGs that are cell type specific
Log2(FC) threshold
$R^2$= 0.74
E
direction
up
down
Astrocyte
Bergmann-glia
Endothelial
Fibroblast
Granule
Interneuron
Microglia
OPC
Oligodendrocyte
Purkinje
Number of cell type specific DEGs

Figure 3. Cell-type-specific transcriptional dysregulation in AT cerebellum.

A. Differentially expressed genes (DEGs) in each cell type with FDR<0.05, |Log2FoldChange|>0.50. Each dot represents a significantly differentially expressed gene. Numbers of upregulated and downregulated DEGs per cell type are shown in red and blue text respectively.
B. Fraction of single-nucleus up and down DEGs per cell type detected by pseudobulk analyses.
C. Proportion of DEGs identified in different numbers of cell types.
D. Proportion of cell-type-specific DEGs at increasing Log2FoldChange thresholds for DEG identification.
E. Number of cell-type-specific up and down DEGs for each cell type.

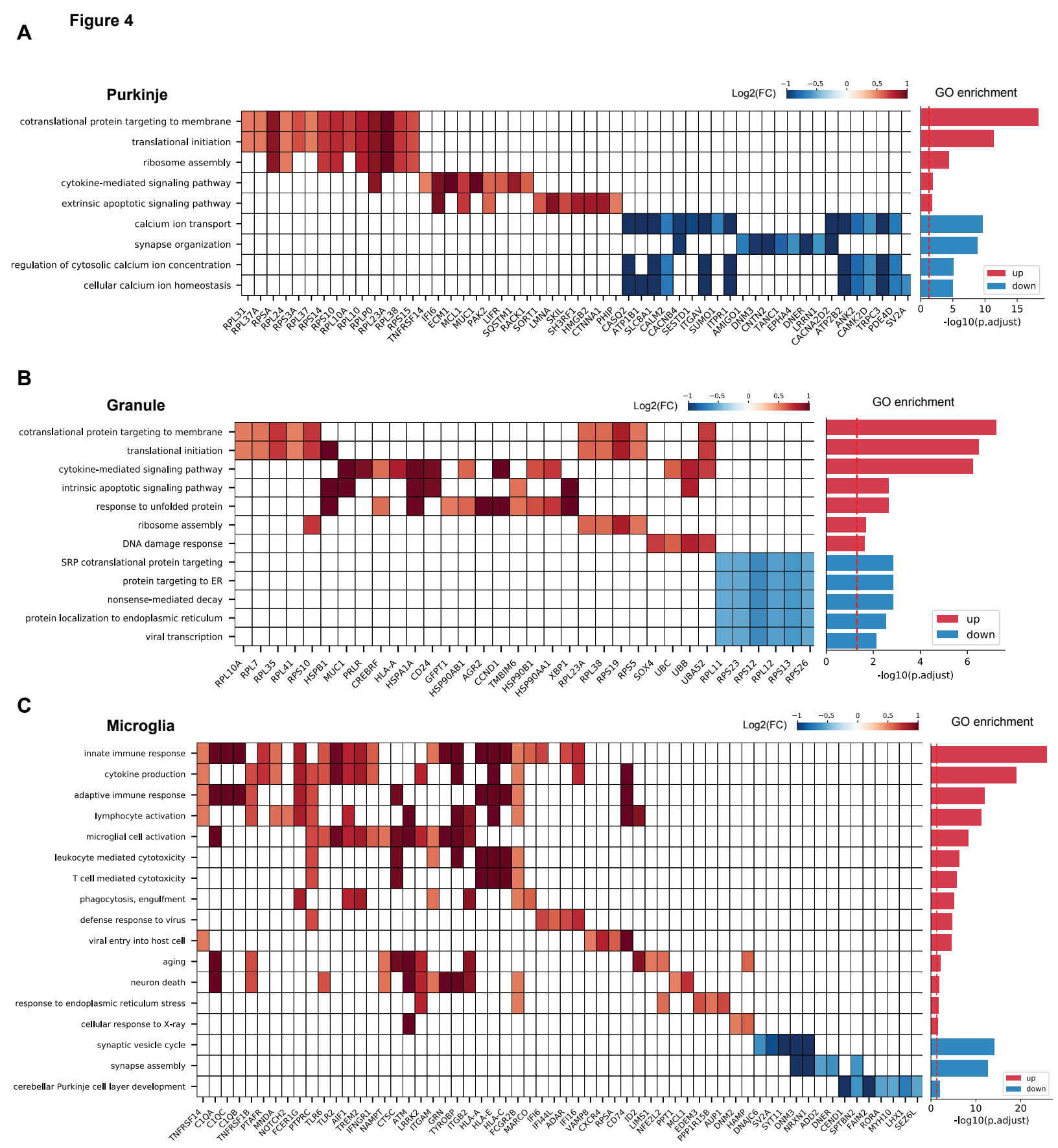


Figure 4. Gene Ontology (GO) analysis of differentially expressed genes in AT cerebellum.
A. Select enriched GO biological processes among DEGs in AT Purkinje neurons. Select genes in each pathway and their log2 fold-changes (AT/control) shown in the heatmap. Barplot shows significance of pathway enrichment.
B. Select enriched GO biological processes among DEGs in AT granule neurons. Select genes in each pathway and their log2 fold-changes (AT/control) shown in the heatmap. Barplot shows significance of pathway enrichment.
C. Select enriched GO biological processes among DEGs in AT CB microglia. Select genes in each pathway and their log2 fold-changes (AT/control) shown in the heatmap. Barplot shows significance of pathway enrichment.

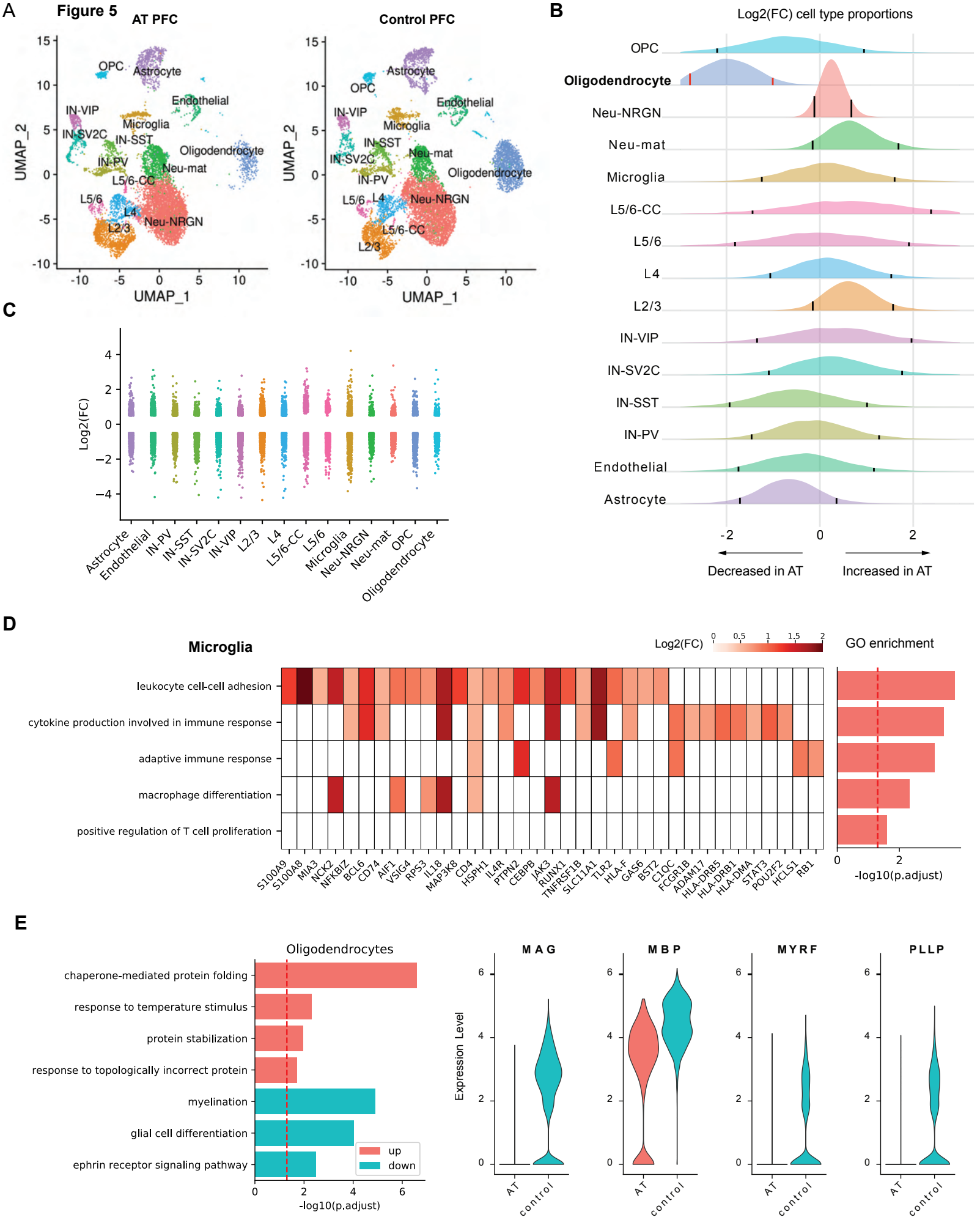
A
Figure 5
AT PFC
Control PFC
OPC
Astrocyte
Endothelial
IN-VIP
Microglia
IN-SV2C
IN-SST
Oligodendrocyte
IN-PV
Neu-mat
L5/6-CC
L5/6
L4
L2/3
Neu-NRGN
UMAP_1
UMAP_2
B
Log2(FC) cell type proportions
Oligodendrocyte
Decreased in AT
Increased in AT
C
Log2(FC)
D
Microglia
Log2(FC)
GO enrichment
leukocyte cell-cell adhesion
cytokine production involved in immune response
adaptive immune response
macrophage differentiation
positive regulation of T cell proliferation
-log10(p.adjust)
E
Oligodendrocytes
chaperone-mediated protein folding
response to temperature stimulus
protein stabilization
response to topologically incorrect protein
myelination
glial cell differentiation
ephrin receptor signaling pathway
up
down
-log10(p.adjust)
MAG
MBP
MYRF
PLLP
Expression Level
AT
control

Figure 5. Cell-type-specific transcriptional dysregulation in AT PFC.

A. UMAP plot of major cell types in AT and control human PFC, downsampled to 10,000 cells per condition.
B. Relative abundance of cell types in AT versus control PFC, shown as the posterior distribution of Log2(proportion in AT/proportion in control) with 89% credible interval. Red bars highlight credible intervals that do not overlap 0. Bolded cell type labels indicate a significant difference in relative abundance.
C. Differentially expressed genes (DEGs) in each cell type with FDR<0.05, |Log2FoldChange|>0.50. Each dot represents a significantly differentially expressed gene.
D. Select enriched GO biological processes among DEGs in AT PFC microglia. Select genes in each pathway and their log2 fold-changes (AT/control) shown in the heatmap. Barplot shows significance of pathway enrichment.
E. Select enriched GO biological processes among DEGs in AT PFC oligodendrocytes. Violin plot of normalized expression of myelination genes *MAG*, *MBP*, *MYRF*, and *PLLP* in AT and control PFC oligodendrocytes.

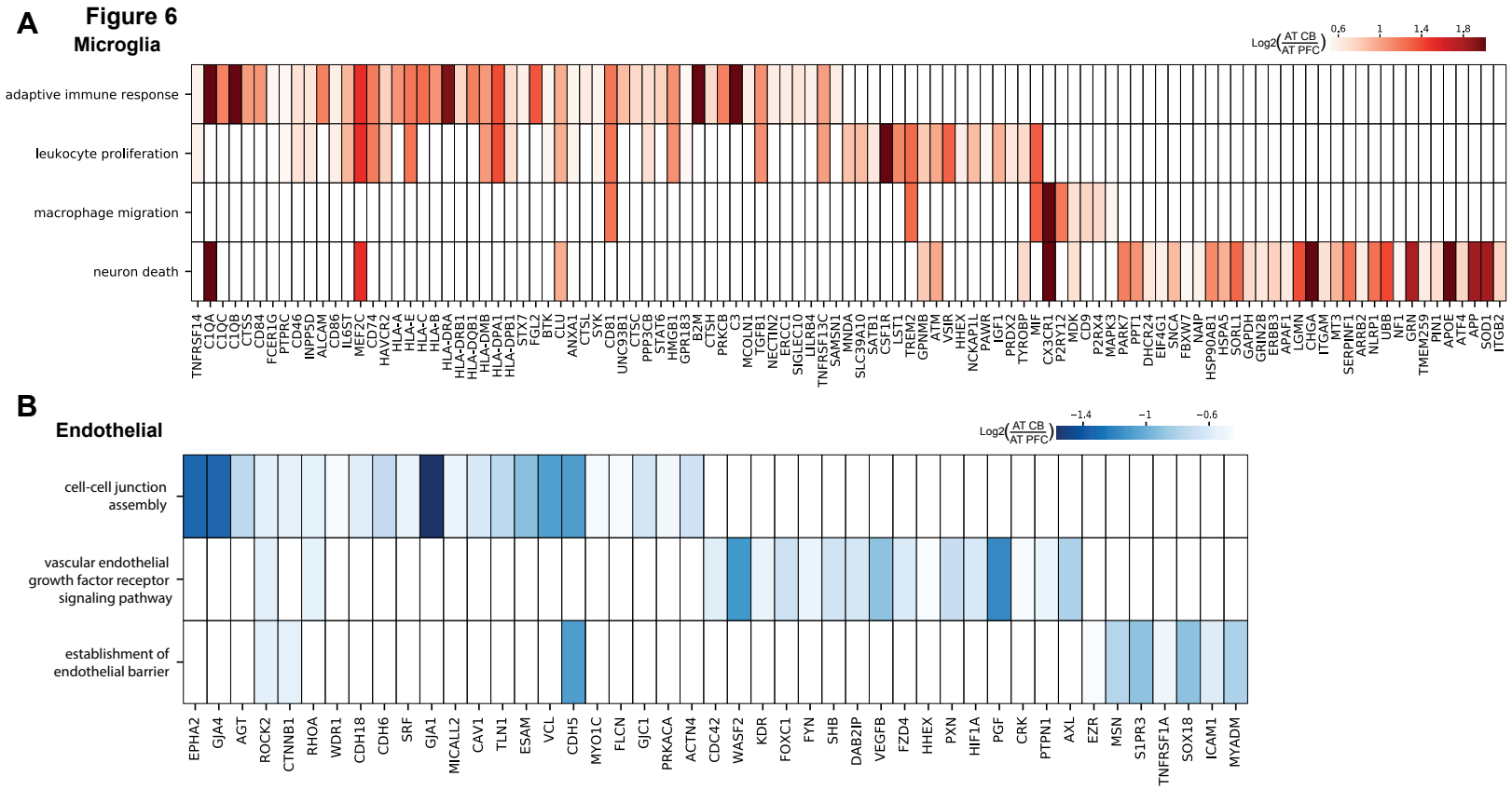


Figure 6. Stronger activation of microglia in AT cerebellum compared to PFC.
A. Heatmap showing enriched GO biological processes and log2 fold-changes of significant DEGs in each pathway with greater upregulation in AT CB microglia than AT PFC microglia.
B. Heatmap showing enriched GO biological processes and log2 fold-changes of significant DEGs in each pathway with greater downregulation in AT CB endothelial cells than AT PFC endothelial cells.
C. CD11B immunostaining of postmortem cerebellar cortex from AT and controls. Red: CD11B. Green: GFAP. Blue: DAPI. WM: white matter. GL: granule layer. ML: molecular layer. Quantification of CD11B immunostaining across cerebellar cortex layers in AT and control. ****Bonferroni-adjusted p-value<1e-04, Mann-Whitney U test.

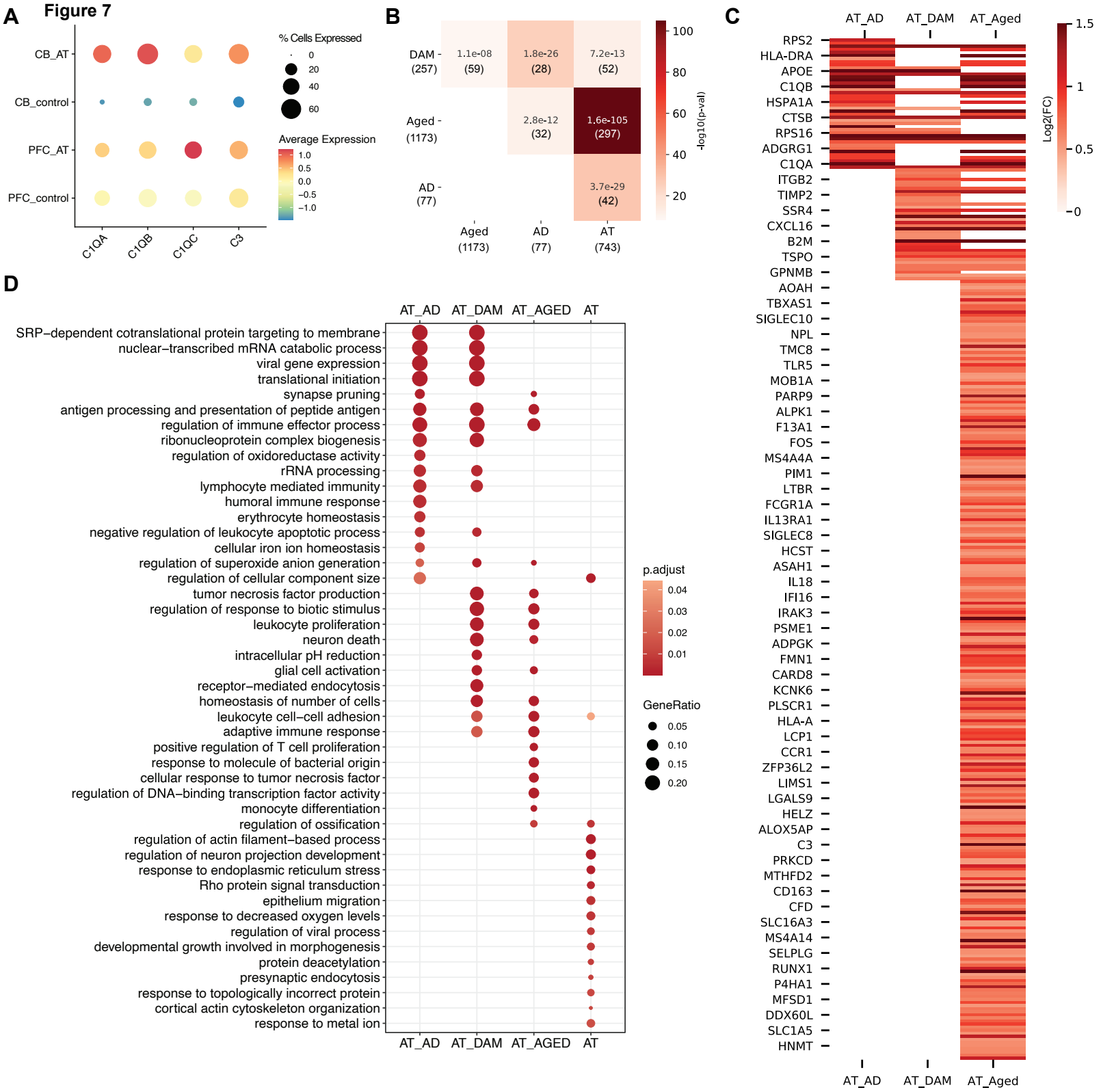


Figure 7. AT cerebellar microglia upregulate markers of aging and neurodegenerative microglia.
A. Average scaled expression of complement components C1QA, C1QB, C1QC, C3 in microglia from AT and control cerebellum.
B. Overlap between AT microglia (AT) upregulated genes and human Alzheimer's disease microglia markers (AD, Mathys et al., 2019), Disease Associated Microglia markers (DAM, Keren-Shaul et al., 2017), and human aging microglia markers (Aged, Olah et al., 2018). Overlap p-values from Fisher's exact test shown in each cell. Color represents -log10(overlap p-value). Number of genes in each set and intersection shown in parentheses.
C. Heatmap of AT microglia log2 fold-changes (FDR<0.05) for overlapping microglia markers. AT_AD: AT and Alzheimer's disease microglia overlapping genes. AT_DAM: AT and DAM overlapping genes. AT_AGED: AT and human aging microglia overlapping genes.
D. GO biological process enrichment of overlapping microglia markers. AT: AT microglia only upregulated genes. Pathways with FDR<0.05 shown.

Figure 8

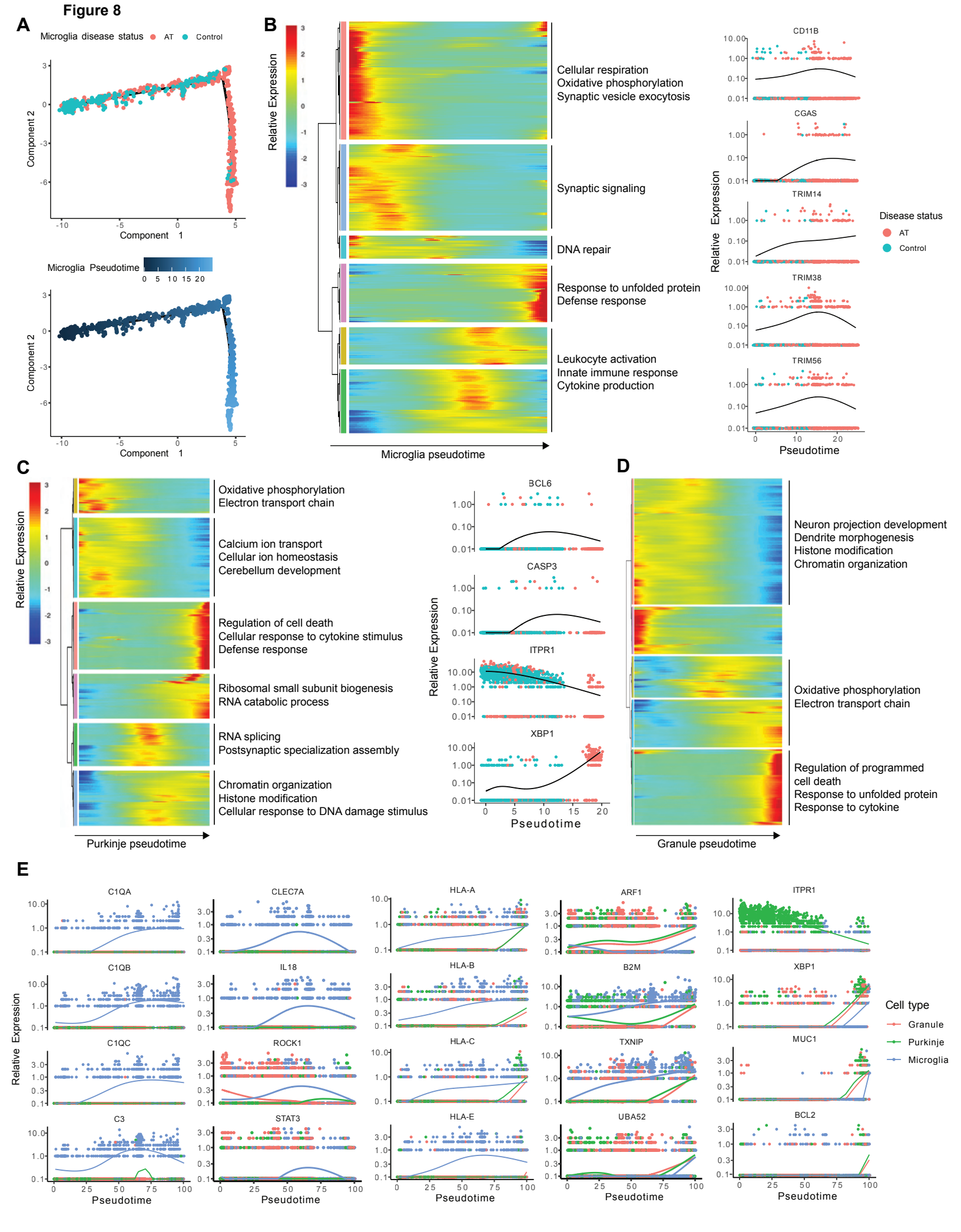
A
Microglia disease status
AT
Control
Component 2
Component 1
Microglia Pseudotime
B
Relative Expression
Cellular respiration
Oxidative phosphorylation
Synaptic vesicle exocytosis
Synaptic signaling
DNA repair
Response to unfolded protein
Defense response
Leukocyte activation
Innate immune response
Cytokine production
Microglia pseudotime
CD11B
CGAS
TRIM14
TRIM38
TRIM56
Pseudotime
Disease status
AT
Control
C
Oxidative phosphorylation
Electron transport chain
Calcium ion transport
Cellular ion homeostasis
Cerebellum development
Regulation of cell death
Cellular response to cytokine stimulus
Defense response
Ribosomal small subunit biogenesis
RNA catabolic process
RNA splicing
Postsynaptic specialization assembly
Chromatin organization
Histone modification
Cellular response to DNA damage stimulus
Purkinje pseudotime
BCL6
CASP3
ITPR1
XBP1
D
Neuron projection development
Dendrite morphogenesis
Histone modification
Chromatin organization
Oxidative phosphorylation
Electron transport chain
Regulation of programmed cell death
Response to unfolded protein
Response to cytokine
Granule pseudotime
E
C1QA
CLEC7A
HLA-A
ARF1
ITPR1
C1QB
IL18
HLA-B
B2M
XBP1
C1QC
ROCK1
HLA-C
TXNIP
MUC1
C3
STAT3
HLA-E
UBA52
BCL2
Cell type
Granule
Purkinje
Microglia

Figure 8. Pseudotime analysis of disease progression reveals early microglia activation.

A. Disease progression pseudotime trajectory of AT cerebellar microglia, colored by disease status (red: AT, blue: control), or pseudotime (healthy to diseased).
B. Heatmap of genes that significantly change over pseudotime in microglia, clustered by pseudotemporal expression patterns. Each cluster is annotated with enriched GO terms (FDR<0.05). Expression of *CD11B, CGAS, TRIM14, TRIM38,* and *TRIM56* over pseudotime in microglia.
C. Heatmap of genes that change over pseudotime in Purkinje neurons, clustered by pseudotemporal expression patterns. Each cluster is annotated with enriched GO terms (FDR<0.05). Expression of *BCL6, CASP3, ITPR1,* and *XBP1* in Purkinje neurons over pseudotime.
D. Heatmap of genes that change over pseudotime in granule neurons, clustered by pseudotemporal expression patterns. Each cluster is annotated with enriched GO terms (FDR<0.05). Heatmaps in b, c, d depict center and scaled expression.
E. Expression of select genes over aligned pseudotime in microglia, Purkinje and granule neurons, showing a rise in inflammatory markers in microglia preceding the rise in ER stress and apoptotic markers in Purkinje and granule neurons.